Preservation of Organic Carbon in Dolomitized Cambrian Stromatolites and Implications for Microbial Biosignatures in Diagenetically Replaced Carbonate Rock

ASHLEY E. MURPHY[a*], SCOTT T. WIEMAN[b,c,d], JULIANE GROSS[e], JENNIFER C. STERN[c], ANDREW STEELE[f], and MIHAELA GLAMOCLIJA[a]

[a]*Rutgers University, Department of Earth and Environmental Sciences, 101 Warren St, Smith Hall – Room 135, Newark, NJ, 07102 (*corresponding author e-mail: ashley.murphy@rutgers.edu)*

[b]*Center for Space Sciences and Technology, University of Maryland, Baltimore, MD 21250, USA*

[c]*Planetary Environments Laboratory, NASA Goddard Space Flight Center, Greenbelt, MD 20771, USA*

[d]*Center for Research and Exploration in Space Science and Technology, NASA Goddard Space Flight Center, Greenbelt, MD 20771, USA*

[d]*Department of Earth and Planetary Sciences, Rutgers University, New Brunswick, NJ 08854, USA*

[f]*Geophysical Laboratory, Carnegie Institution of Washington, Washington, DC, 20015, USA*

ABSTRACT

Stromatolites have been a major focus in the search for ancient microbial biosignatures, in particular, stromatolites containing silicified microfossils. Silicification allows for the preservation of original textures and morphologies, which are important starting criteria in the characterization of fossils' biogenicity and syngenicity to host rock. The microbial biosignatures of dolomitized stromatolites have not yet been characterized and correlated with their dolomitizing conditions. The Cambrian Allentown Formation in New Jersey is an excellent example of dolomitized stromatolites and thrombolites containing diagenetically modified microbial biosignatures. Based on XRD, ICP-OES, and EPMA data, the dolomite is ordered, and all three generations of dolomite are stoichiometric. The outcrop underwent early dolomitization by meteoric diagenesis and burial diagenesis resulting in multi-generational dolomite formation as follows: (1) The microspar dolomite formed by early replacement of precursory calcium carbonate minerals, at or very near the surface, where mixing of fresh and marine waters produced finely crystalline dolomite, (2) The zoned dolomite formed penecontemporaneously with the microspar phase as rhombohedral crystals by infilling primary pore spaces within the microspar matrix. Cloudy cores observed in many larger dolomite rhombs indicate recrystallization before the crystals grew outward in alternating stages, preserved in zoned rims, of Fe-enriched and -depleted fluids, (3) The saddle dolomite formed during late stage deeper burial with Fe- and Mn-rich fluids and occurs as void-filling, high-temperature phase. Organic carbon, characterized using confocal Raman microscopy, is exclusive to first generation microspar dolomite, and the D and G bands' characteristics reveal similar style thermal alteration as host rock, indicating that the mapped organic carbon is syngenetic with the Cambrian stromatolites. This study offers a new way to investigate ancient life signatures preserved in secondary dolostones and may aid biosignature detection in ancient carbonate rocks on Mars.

Keywords: dolomitization, Cambrian stromatolites, organic carbon, biosignature, meteoric diagenesis, burial diagenesis

1. INTRODUCTION

Stromatolites are microbially mediated sedimentary structures that record the oldest forms of life on Earth (Barghoorn and Tyler, 1965; Grotzinger and Knoll, 1999; Allwood et al., 2006). These ancient structures have been a significant focus of both geo- and astrobiology because silicification during early diagenesis provides exceptional preservation of original textures and organic chemistry, which are the leading indicators in the characterization of biogenicity and syngenicity (Knoll et al., 1988; Buick, 1990; Grotzinger and Knoll, 1999; Van Kranendonk et al., 2003; Sugitani et al., 2007; Schopf and Kudryavtsev, 2012; Braiser et al., 2015). Unlike silicification, dolomitization commonly results in the loss of original microstructural details of microbial fossils (Schopf, 1999; Bartley et al., 2000), making the characterization of syngenetic and indigenous biosignatures ambiguous (Grotzinger and Rothman, 1996). As the calcium carbonate grains solidify to limestone, the developing crystals press the microorganisms between grain boundaries as they grow, thereby destroying cellular morphology (Schopf, 1999).

Although studies of biosignatures in dolomitic stromatolites have been reported, they have been interpreted as primary dolomite precipitation (Rao et al., 2003; Ayllón-Quevedo et al., 2007; Sanz-Montero et al., 2008; Calça et al., 2016) within which fossils were preserved exclusively in silica (Ayllón-Quevedo et al., 2007; Sanz-Montero et al., 2008; Calça et al., 2016) or sulfur-rich mineral phases (Lindtke et al., 2011). The effects of dolomitization, as a secondary process when devoid of silicification, on the preservation of microbial biosignatures, have yet to be thoroughly interpreted. The identification and characterization of indigenous and syngenetic biosignatures preserved in a host rock that has undergone secondary dolomitization alteration are complicated due to loss of the original microbial morphologies. Although the original texture is commonly obliterated by later replacement and recrystallization processes, dolomitization settings vary, and some of the temperature and pressure parameters associated with it may be conducive to the long-term preservation of the indigenous organics. The syngenicity of this type of fossilization in the geologic record can only be comprehensively examined after the degree of alteration of the host rock has been appropriately characterized and evaluated against that of the biologic remains.

The gap in knowledge of dolomitized microbial biosignature preservation is further complicated when applied to astrobiology. Carbonate lithologies are a recognized astrobiology target for Mars exploration, and the primary science goal of the Mars 2020 mission is to determine whether life existed on Mars by seeking signs of extinct life in the rock record (Mustard et al., 2013). Although the origin of the magnesium carbonates identified at the Martian paleolake Jezero Crater (~4-3.5 Ga) is still uncertain (Ehlmann et al., 2008; Goudge et al., 2015), the crater may contain lacustrine carbonate deposits (Horgan et al., 2020) which are habitable environments on Earth that are capable of biosignature preservation. Therefore, terrestrial analogs of ancient magnesium carbonates, such as dolostone, will allow for better interpretation of potential biosignatures in Martian carbonates.

In this paper, measurements of whole rock, bulk carbonate, and high-resolution in situ analysis of each generation of dolomite is used to characterize the dolomitization setting to evaluate the level of diagenetic alteration that has affected the analyzed stromatolitic outcrop, and the effect such alteration had on the preservation of indigenous microbial biosignatures within these Cambrian carbonates.

2. GEOLOGIC SETTING

2.1. Regional geology and sedimentology

The Late Cambrian (515-500 Ma) Allentown Formation (Weller, 1903; Howell, 1945; Harris et al., 1995; Dalton et al., 2014), commonly referred to as Allentown Dolomite, is part of the Kittatinny Supergroup (542-443 Ma) which is a northeast-trending belt (Fig. 1 B) that records the formation of the eastern Laurentian passive margin, when the deposition of shallow-water carbonates dominated, and sediments from eroding inland rocks were transported by streams to the coast and deposited on the shallow shelf (Miller, 1941; Dalton et al., 2014).

Paleoreconstruction of the area shows the ancient North American landmass, Laurentia, positioned below the equator and rotated approximately 90° clockwise from its current orientation.

The paleoenvironment has been interpreted as a shallow subtidal to supratidal setting dominated by limestone deposition that later dolomitized (Miller, 1941; Stead and Kodama, 1984; Dalton et al., 2014). The Taconic orogeny of the Late Ordovician period (~440 Ma) is recorded in the uplift, folding, and faulting in the region, which was further deformed by the Alleghanian orogeny during the Permian period (~270 Ma) (Miller, 1941; Drake, 1965; Dalton et al., 2014).

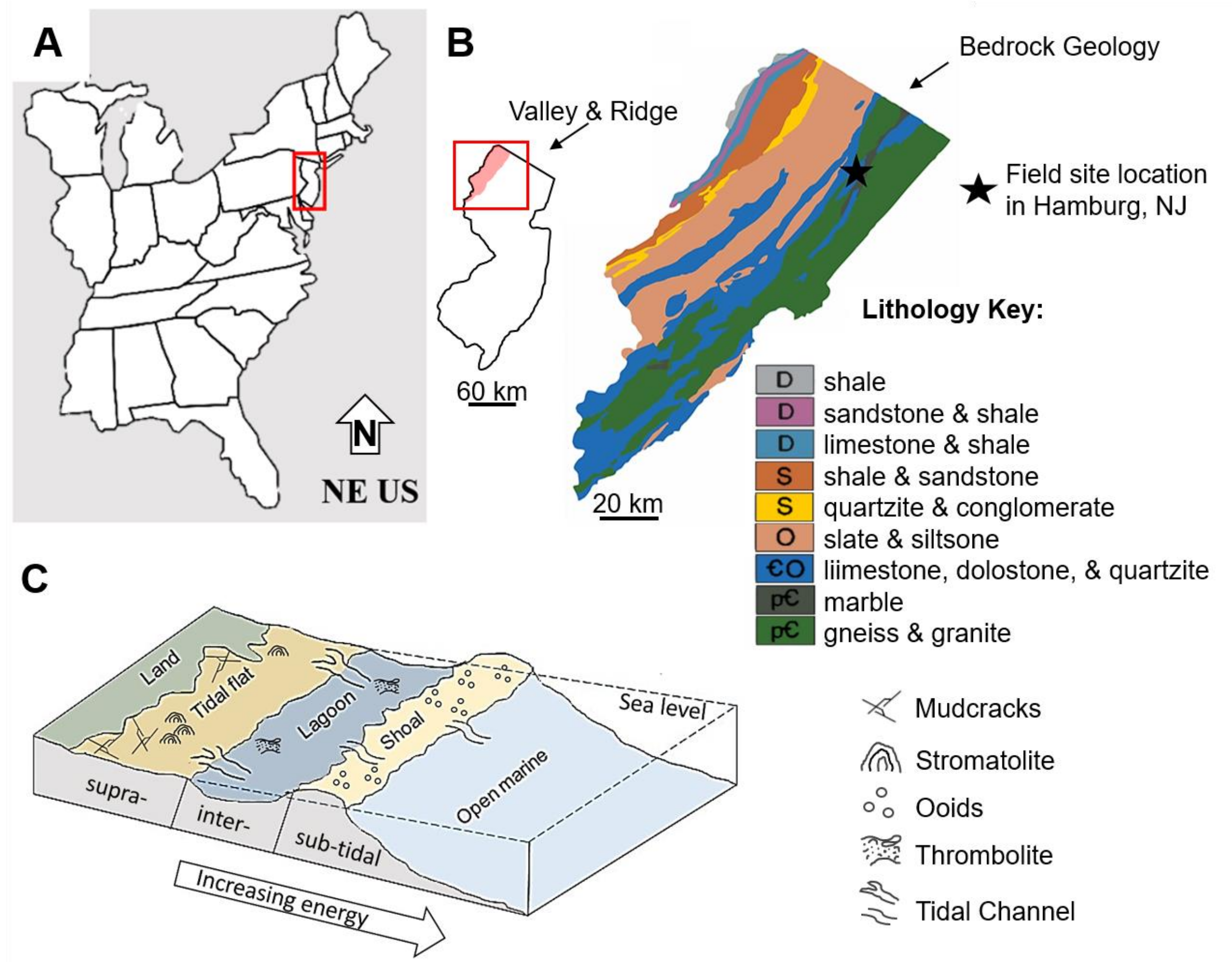

Fig. 1. Geologic map and sampling location. (A) Location of New Jersey (NJ) within the United States of America. (B) Location of the studied Allentown Formation outcrop (marked by star) in Hamburg, NJ. The Cambrian to Middle Ordovician Kittantinny Supergroup (blue lithology) of the Valley and Ridge Physiographic Providence in NJ (red shaded area within red box of inset NJ map). Modified from Witte and Monteverde (2012). (C) Reconstruction of paleoenvironment based on outcrop observations in this study. Modified from Pratt et al. (1992).

Previous geologic mapping of the Allentown formation reveals that the bedding varies (from oldest to youngest) as follows: textureless dololutite (<0.0039 mm grain size), dolarenite (0.0625-

2 mm), oolitic dolarenite (0.0625-2 mm), dolorudite (>2 mm), cryptozoan dolomite, and desiccation dolorudite (>2 mm) (Drake Jr., 1965). In areas of large exposure, these beds repeat in a cyclic manner, where individual cycles range in thickness from ~2 to 10 m, and the entire formational sequence measures up to 580 m thick (Drake Jr., 1965; Monteverde, D.H., 1992). In the 1950s, the Allentown was referred to as two members, (from bottom to top) the Limeport and Allentown members (Drake Jr., 1965). This distinction was made in older literature because the lower Limeport member contains numerous ‘cryptozoan’ (hereafter referred to as stromatolites) of various morphologies, including large domes with convex-shaped laminae, wavy beds, and small domes of laterally linked lamina (Drake Jr., 1965).

2.2. Study area

The study area in Hamburg, New Jersey is 40 m of uplifted dolostone, tilted 44° NW. Exposure along the southwestern side of the outcrop (Fig. 2 A and Fig. 3 column A) allows for measurements of bedding thickness that are elsewhere inexact due to glacially polished rock surfaces. Along the longest transect, the outcrop is 100 m long with extensive vegetation cover that limits correlation between the northeast and southwest parts of the outcrop (Fig. 3). The transect analyzed in the middle of the outcropping area (Fig. 3 column B) includes before mentioned stromatolites. The bottom of the transect is ~13 m of fine-grained, grey dolosiltite intercalated with iron oxidized dissolution seams that are weathered black in outcrop (Fig. 2 B). The occurrence of thrombolites is marked by a brown wavy layer of ~1 cm thick laminae (Fig. 2 C). The thrombolites are overlain by small (≤5 cm) round stromatolite heads (Fig. 2 D and E) that continue to occur periodically in overlying strata for ~20 m. Massive oolitic dolarenite (Fig. 2 F) is situated above the stromatolite heads for ~11 m. The oolitic grainstone is overlain by ~13 m of dolosiltite with numerous beds of high energy, storm deposit features such as of rip-up clasts (Fig. 2 G) edgewise conglomerates

(Fig. 2 H), and jumbled intraclasts (Fig. 2 I). These beds co-occur with coarse-grained dolomite-filled vugs (≤9 mm) (Fig. 2 J). Large (≤30 cm) domal stromatolites are observed at the top of the formation and surrounded by intraclasts, and collapse breccia (Fig. 2 K). The NE side of the outcrop reveals the convex up structure of the domes (Fig. 2 L) Mudcracks are situated above the large domal stromatolites (Fig. 2 M) and syneresis cracks are observed southwest of the stromatolites (Fig. 2 N). Wavy stylolites parallel to bedding are found throughout the formation (Fig. 2 O). Chert occurs as black lenses or thin layers (~1 cm) throughout the formation (Fig. 2 P). This bedding sequence corresponds with a shallowing upward peritidal sequence (Fig. 1 C and see 5.1.).

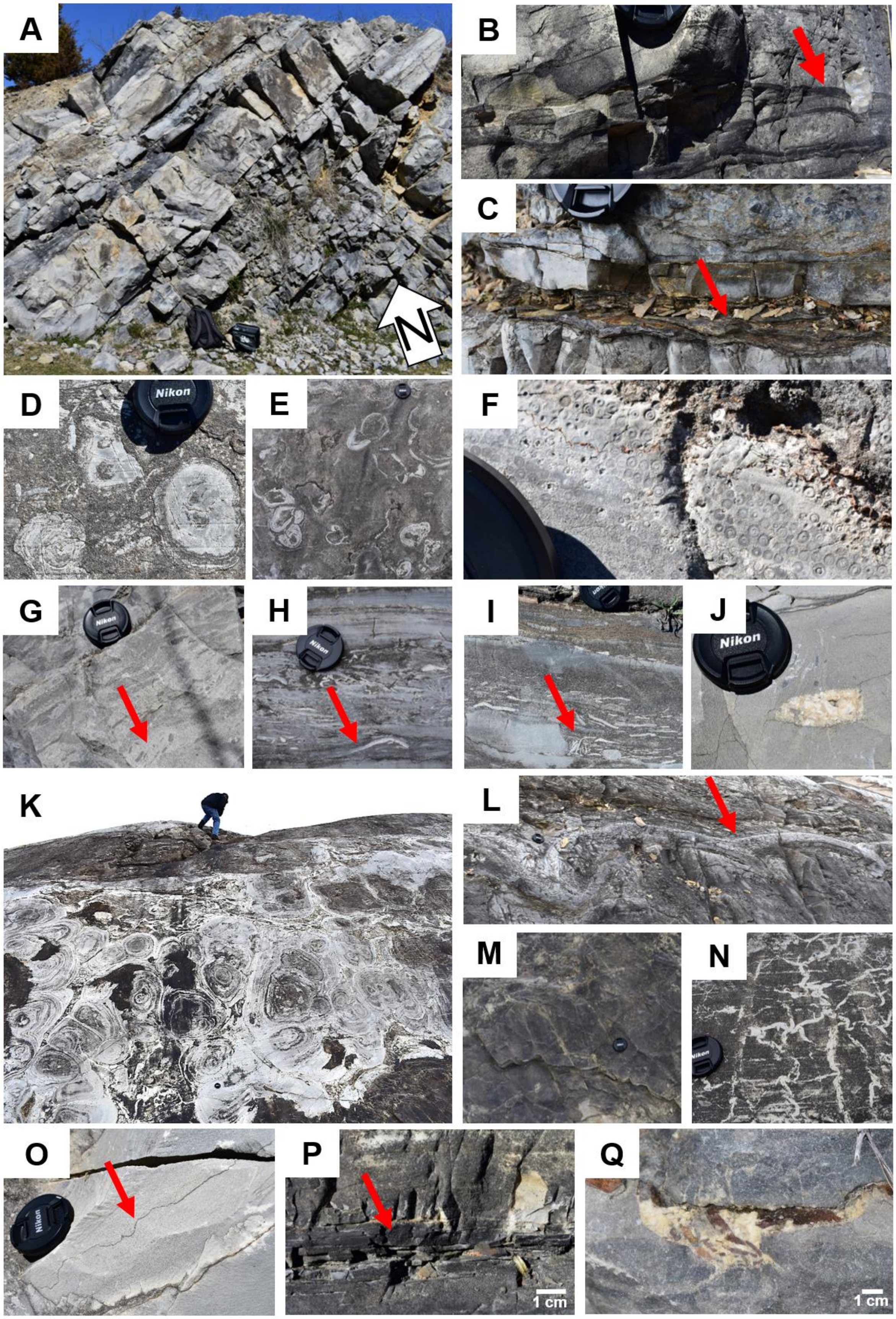
A
B
C
N
D
Nikon
E
F
G
Nikon
H
Nikon
I
J
Nikon
K
L
M
N
Nikon
O
Nikon
P
1 cm
Q
1 cm

142

Fig. 2. (A) Side view of formation with tilted layers dipping 44° NW. (B) Dolosiltite intercalated with solution seams. (C) Brown crinkled layer (red arrow) marks the top of thrombolites (D) Small stromatolite heads. (E) Ripped up stromatolite heads. (F) Ooid grainstone. (G) Dark grey rip-up clasts. (H) Edge-wise conglomerates. (I) Jumbled intraclasts. (J) Large vug filled with coarse-grained dolomite. (K) Top of formation with glacially smoothed domal stromatolites (L) convex upward shape of stromatolites from NE side of outcrop. (M) Mudcracks and (N) syneresis cracks visible from top of formation. (O) Wavy stylolite parallel to bedding. (P) Black chert lens. (Q) Collapsed stylolite material into coarse-grained dolomite filled vug. Nikon camera lens (5.5 cm radius) used for scale.

3. MATERIALS AND METHODS

3.1. Sampling strategy

Samples were collected from 2017 to 2020 in Hamburg, NJ. The sampling strategy included twenty-two different sampling points, from bottom to top of the formation, while targeting obvious stromatolitic morphologies and significant changes in strata texture or appearance. Table 1 lists samples from bottommost (A12d) to the topmost bedding layers (A18). All samples were collected in an organically clean manner to avoid contamination by using gloves to handle samples that were wrapped in sterile aluminum foil and placed in canvas bags. Subsampling was performed in the laboratory using a diamond blade saw and DI water to cut away outer rock layers from the interior areas that were later used for analyses.

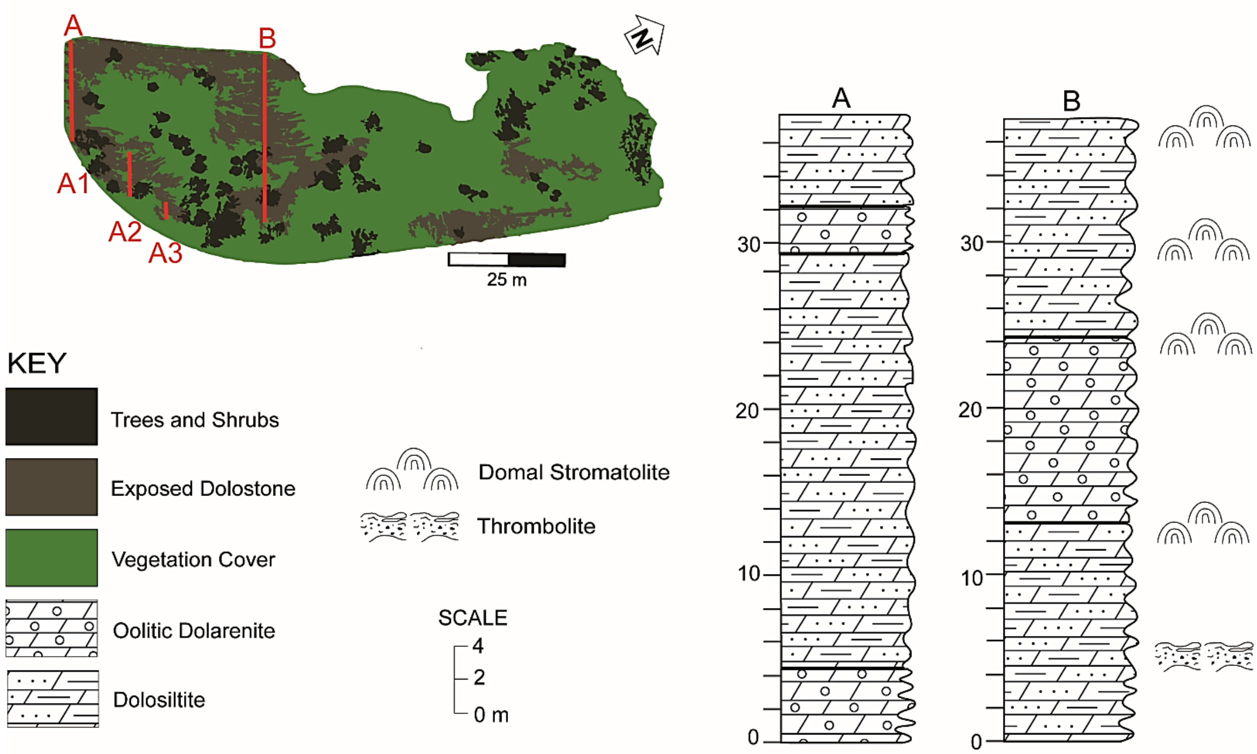

Fig. 3. Stratigraphic columns from sampling area. Column A is exact bedding thickness measured along A1, A2 and A3 (marked red on outcrop figure). Column B is estimated thickness along glacially smoothed bedding measured along B (marked red). Outcrop figure modified from aerial Google Earth imagery. Note the lateral differences in both columns and lack of microbial structures observed at Column A.

3.2. Petrographic and mineralogical analyses

Petrographic analyses of 14 representative layers were used to describe the stromatolites and associated dolostone. The petrographic study involved plane polarized and cross polarized light inspection of thin sections for textural and mineral identification, as well as to target regions of interest for further spectroscopy.

The detection of minor mineral phases was performed by Scanning Electron Microscopy with Energy Dispersive X-ray Spectroscopy (SEM/EDS) using a Hitachi S-4800 operating at 15 to 20 kV and 12 to 15 uA, equipped with an Apollo X EDAX at Rutgers University in the Department of Chemistry.

Qualitative elemental X-ray mapping and cathodoluminescence (CL) mapping was performed on 6 thin sectioned samples with an accelerating voltage of 15 kV, a beam current of 14 nA, a beam diameter of 1 micron, with a 1 μm step size per pixel and 30 ms dwell time. Equipment used was a JOEL Superprobe JXA-8200 at Rutgers University in the Department for Earth and Planetary Sciences.

Powder X-ray diffraction (XRD) of whole rock samples was used to determine dominant mineral assemblages in 21 samples. The equipment used was a Bruker D8 at Rutgers University in the Department of Earth and Environmental Sciences. Operational settings were 40 kV, 25 mA, and Cu-Kα radiation. Quantitative analysis of stoichiometry was determined by the 2Θ value of the d_{104} peak in order to calculate the d-spacing using Bragg's Law (Bragg and Bragg, 1913). The degree of cation ordering was determined by the intensity ratio of the d_{015} and d_{110} peak (Graf and Goldsmith, 1956).

3.3. Geochemical analyses

The $\delta^{13}C_{dolo}$ and $\delta^{18}O_{dolo}$ of 16 bulk and 7 micro-drilled samples were determined for further analyses of the origin of dolomite. The bulk samples were prepared and analyzed in triplicate. The 7 micro-drilled samples were sampled from thin-section billets using a Medenbach© microdrill at Rutgers University in the Department of Earth and Planetary Sciences in order to isolate microspar and saddle dolomite generations for comparison to the bulk rock, and to target the minimum and maximum temperatures of formation. The micro-drilled samples were analyzed in, at minimum, two replicates.

Isotope Ratio Mass Spectrometry (IRMS) was used to determine the carbonate diagenetic setting using a GasBench II System coupled to a Delta V Plus IRMS at NASA Goddard Space Flight Center in the Planetary Environments Laboratory. CO_2 was evolved from each sample at

60°C using 85% H_3PO_4. Samples were acidified in 6N HCl for approximately 48-96 hours and analyzed for organic carbon abundance, nitrogen abundance, and $\delta^{13}C_{org}$ using an Elemental Analyzer coupled to a Delta V Plus IRMS at NASA Goddard Space Flight Center in the Planetary Environments Laboratory.

Electronprobe Microanalyses (EPMA) were carried out using the JOEL Superprobe JXA-8200 at Rutgers University in the Department for Earth and Planetary Sciences. Quantitative spot analyses to isolate each generation of dolomite was performed on 6 samples using an accelerating voltage of 15 kV, a beam current of 15 nA, and a beam diameter of 5 microns.

Chemical analyses of 16 samples using Inductively Coupled Plasma - Optical Emission Spectroscopy (ICP-OES) was carried out at Rutgers University in the Department of Earth and Environmental Sciences to access the bulk carbonate concentration of major (ppm) and trace (ppb) cations using an Agilent 5510. The digestion method used was based on the EPA procedure 3052. All samples were analyzed in triplicate, and average values are reported.

3.4. Confocal Raman microscopy and thermometry

Confocal Raman Microscopy and Spectroscopy was used for spot analyses and mapping of 14 thin sections and 8 unprocessed rock samples, to determine the organic carbon spatial distribution, associations with minerals, and to analyze the D and G bands (~1350 and 1600 cm^{-1}, respectively) characteristic Raman signal for the organic matter. Five thin sections were chosen for the final high-resolution analysis, these representative layers ranged across the top, middle, and bottom areas of the outcrop and include all lithological textures observed at the outcrop. This work was performed with a WITec alpha300 equipped with a frequency-doubled Nd:YAG (532 nm) excitation laser. Operational settings were as follows: a 1 mV average laser intensity (range from 1-3 mV) to minimize laser-induced heating and to avoid structural modification of the samples, and a depth of 1-5 μm below the surface to was used to avoid surface contamination. Mapped areas were visually inspected by transmitted and reflected light microscopy for holes and cracks in the samples that may contain polishing grit, epoxy, or other contaminants related to sample handling that may interfere with the D and G band spectra. Samples that could not be unambiguously identified as unaffected by this type of contamination or were too friable for thin sectioning were not included in the final Raman data sets.

D and G bands were analyzed in two ways for data quality assessment, using 1) WITec Project FIVE+ software cluster analysis and, 2) WITec Project FIVE+ software Gaussian fitted background subtraction. The cluster method identifies variations in D and G band phases within a map, averages it, and displays a distribution map. Ten clusters of spectral variations were calculated from each map, and one to three were chosen from each mapped area after quality evaluations (signal-to-noise ratio, surface contamination, and interference bands from hematite were avoided after being inspected both visually and spectrally). The Gaussian fit method uses a Savitzky-Golay filter to smooth the graph before applying background subtraction using a Gaussian fit for both the G and D bands. The average D and G band peak centers are displayed on a distribution map where one to three spectral points, representative of different spectral trends, were hand selected. Maps were inspected for visual and spectral interferences as listed above in the cluster analysis method.

All spectra were normalized to facilitate comparison. Band intensities were normalized by taking the height of each band and dividing it by the most intense G band in the spectrum. Data collected from both methods were exported as ASCII files into Excel and used to calculate the Raman parameters of the D/G intensity ratio, peak area, and the Raman shifted peak position. A two-tailed, two-sample *T*-test (p=0.05) was applied to D and G spectral data to determine if variations within the bands were statistically different. The peak table exported from the WITec software was used to report the full width at half maximum (FWHM) for both D and G bands. Thermometry was calculated using the D1 band geothermometer from Kouketsu et al. (2014):

$$T(°C) = -2.15 * (FWHM\text{-}D1) + 478\ (\pm 30°C)$$

This geothermometer was chosen due to the consistency of FWHM with temperature (Kouketsu et al., 2014) and the spectral characteristics of the Allentown's D and G peaks which do not exhibit an obvious D2 peak within the G peak.

4. **RESULTS**

4.1. Allentown petrology and mineralogy

4.1.1. Bulk mineralogy

Based on Powder X-Ray Diffraction (XRD) (Fig. S1 in supplementary material) the lithology of the Allentown Formation is predominantly dolomitic with few ±1 to 40 cm thick, greyish-black chert lenses, and ±1 cm brown colored feldspathic carbonate layers (samples A15, A15b, and A6, respectively).

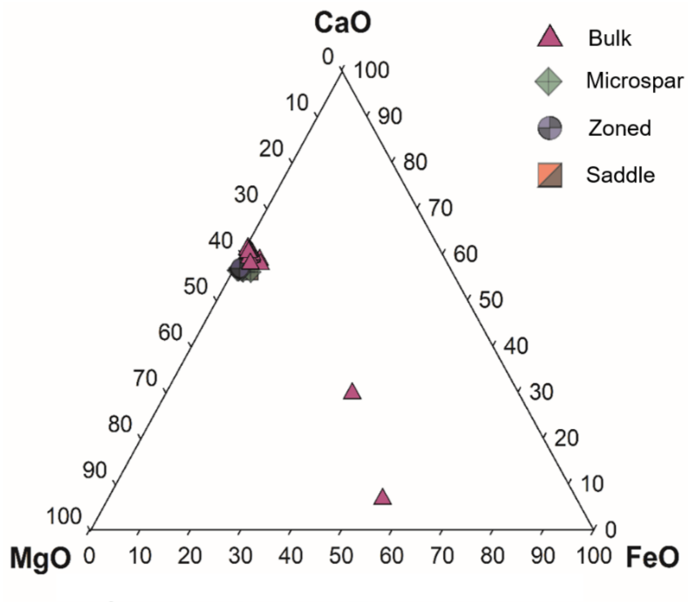

Fig. 4. Ternary diagram comparing stoichiometry from ICP-OES bulk carbonate MgO, CaO, and FeO concentrations (pink triangles) to EPMA measured MgO, CaO, and FeO concentrations for separate dolomite generations (see legend). The two outliers of bulk carbonate composition are the feldspathic (A6) and cherty dolomite samples (A15). All dolomitic samples cluster in the dolomite range of the diagram, near 40 to 45% MgO and 55 to 60% CaO composition.

The feldspathic (orthoclase and microcline) carbonate layers occur as thin wavy layers or disk-shapes and are commonly observed along fractured bedding surfaces or at the top of microbial macrostructures. The average d-spacing of the dolomite d_{104} peak is 2.89 Å (n=21), while the range in degree of cation order calculated by the d_{015}/d_{110} intensity ratio is 0.36 - 0.99 (Table 1). Cherty and feldspathic carbonate samples did not exhibit d peaks of (015) or (110) in XRD, and therefore these samples were not included in the stoichiometry and cation ordering averages.

Sample ID	Sample Description	Degree of Cation Order (d_{015}/d_{110})	Stoichiometry				
			P-XRD d_{104}-spacing	ICP-OES Mg/Ca (ppm)	EPMA (avg. elemental wt %) Micritic	Zoned	Saddle
A18	dolarenite mudcracks	0.654	2.890	-	-	-	-
A17	feldspathic dolarenite tidal channel deposit	0.604	2.888	-	-	-	-
A16	dolosiltite domal stromatolite	0.599	2.886	0.566	0.621	0.620	0.602
A15a	chert lens	n/a	n/a	4.800	-	-	-
A14	oolitic dolosiltite	0.659	2.893	0.530	0.621	n/a	0.586
A13	oolitic dolosiltite	0.619	2.893	0.534	-	-	-
A12a	oolitic dolarenite	0.848	2.893	0.530	0.628	0.629	n/a
A11	dolarenite	0.989	2.884	0.537	0.628	0.628	n/a
A10	oolitic dolarenite	0.640	2.893	0.533	0.622	n/a	n/a
A9	oolitic dolosiltite	0.491	2.893	0.529	-	-	-
A8	dolosiltite	0.375	2.893	0.532	-	-	-
A7	oolitic dolosiltite	0.900	2.893	0.527	0.619	0.630	n/a
A6	feldspathic dolosiltite disk	n/a	2.888	0.939	-	-	-
A5	oolitic dolosiltite thrombolite	0.596	2.885	0.525	-	-	-
A4	dolosiltite	0.737	2.894	0.529	-	-	-
A3	dolosiltite with microstyolites	0.683	2.893	0.525	0.618	0.625	n/a
A2	dolosiltite with solution seams	0.363	2.894	0.551	-	-	-
A1	dolosiltite with solution seams	-	-	0.543	-	-	-
A15b	dolomitic chert lens	n/a	2.854	-	-	-	-
A12b	oolitic dolarenite	0.656	2.889	-	-	-	-
A12c	oolitic dolarenite	0.772	2.891	-	-	-	-
A12d	oolitic dolarenite	0.788	2.890	-	-	-	-

dolosiltite = silt sized grains (5 µm - 63 µm) n/a denotes no data from analysis
dolarenite = sand sized grains (63 µm - 2 mm) - denotes the sample was not analyzed

Table 1. Stoichiometry and cation order within samples listed from bottommost to topmost sampled strata, A12d to A18, respectively. Cation order ranges from 0.36 – 0.99 and indicates the Allentown dolomite is relatively well to well ordered. Values from XRD d-spacing, ICP-OES and EPMA Mg/Ca ratios all indicate the Allentown dolomite is stoichiometric.

4.2. Microtextures and mineralogy

4.2.1. Multi-generational dolomite characterization

Composite Red-Green-Blue (RGB) cathodoluminescence maps with R = 450-500 nm, Green = 400-450 nm, and Blue = 350-400 nm reveals three distinct generations of dolomite in all analyzed samples. Dolomite generations vary in crystal size, shape, and intercrystalline boundaries. Based on the nomenclature from Sibley and Gregg (1987), the three generations of dolomite are classified and characterized from oldest to youngest as microspar, zoned, and saddle. The microspar dolomite is nonplanar, has closely packed anhedral crystals with irregular, intercrystalline grain boundaries. The crystals average 20 microns and range 5-40 microns in size.

Zoned dolomite is planar, subhedral to anhedral medium grained (10-100 microns) with straight compromised boundaries. The crystals are concentrically zoned in CL and characteristically pore lining or void-filling (Fig. 5 E and Fig. 6). Saddle dolomite is nonplanar, medium (10-100 microns) to coarse grained (>100 microns) saddle-shaped, void-filling, and exhibits undulatory extinction in cross polarized light (Fig. 7 A3 and A4). The three observed CL colors, by increasing wavelength are blue, grey, and gold, and are found throughout the zoned and microspar dolomite generations; the saddle dolomite exhibits a dull bluish color in CL. Throughout each generation of dolomite, two CL spectral peaks are present at 389 nm and 650 nm.

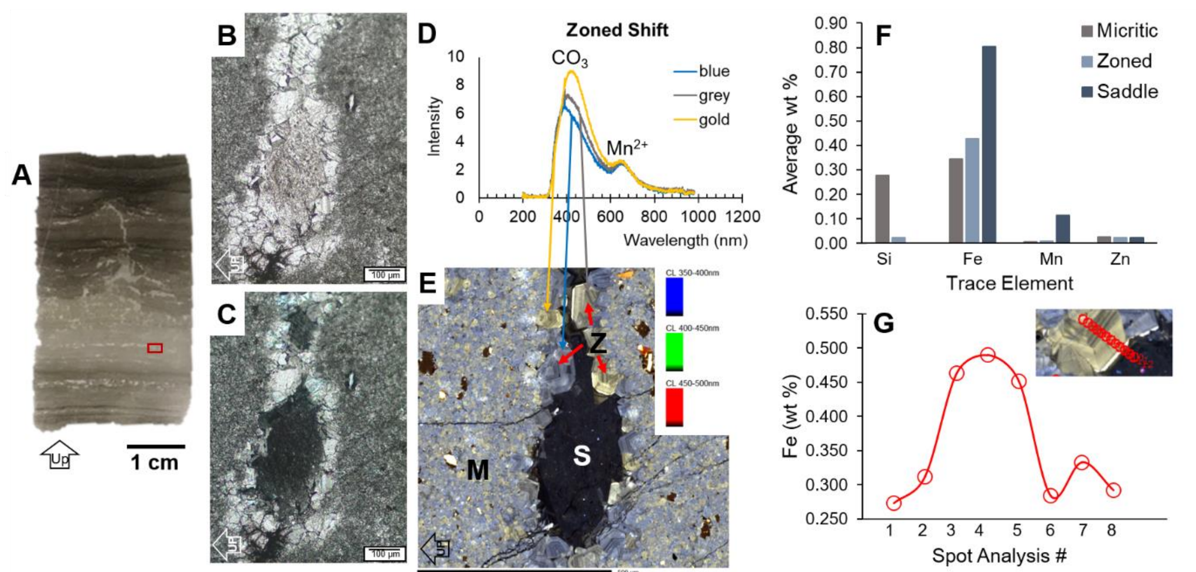

Fig. 5 CL and EPMA results. (A) Thin section of domal stromatolite. Red box indicates mapped area in (E). (B) Plane polarized light photomicrograph of fenestral pore from sample (A). (C) Cross polarized light photomicrograph of (B). (D) Characteristic spectra of luminescence colors showing a peak shift at CO_3. (E) CL map showing three generations of dolomite: microspar (M), zoned (Z), and saddle (S). (F) EPMA spot analyses across each generation of dolomite showing the dolomitizing fluid compositional changes. (G) EPMA spot analysis across zoned dolomite reveals dark zonation bands are Fe-enriched.

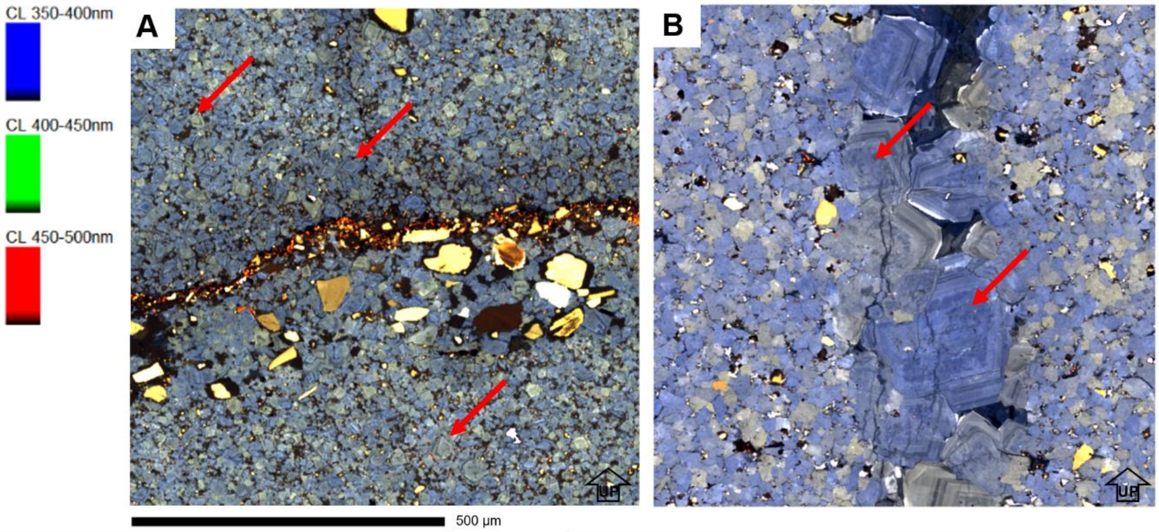

Fig. 6 (A) CL map of microstylolite from dolosiltite sample A3 showing zoned rhombohedral dolomite in pores of the microspar dolomite matrix (red arrows). Numerous feldspars (larger yellow-brown grains) can be seen near the solution seam. (B) CL map of vertical microfracture in dolarenite sample A11 showing zoned dolomite that lines and fills the microfracture. The rhombohedral dolomite cores appear cloudy (red arrows), indicating recrystallization.

4.2.2. Porosity types and dissolution features

Open porosity is absent in the studied samples, but occluded pore types of primary and secondary origins were observed. Primary fenestral porosity (≤1 mm in size) is ubiquitous in stromatolite samples and infilled with zoned and saddle dolomite (Fig. 8 B1, B3, and B4). Secondary microfractures occur in two stages. The first stage includes vertical microfractures (<1 mm wide), infilled with zoned and saddle dolomite, that are present in limited layers of microspar dolomite, and crosscut horizontal laminae and fenestrae in the domal stromatolite (Fig. 8 A3). The second stage includes randomly oriented microfractures (<1 mm wide) that are present in the oolitic dolosiltite sample A14 and are only infilled with saddle dolomite. Vugs are large secondary pores that are at least two times greater in size than the microspar matrix, the vugs are in average 2 mm to 9 mm in size and are infilled with zoned and saddle dolomite (Fig. 2 J). Vugs occur predominately in storm layers with rip-up clasts and are absent from the lowermost lagoonal facies.

Dissolution structures of numerous solution seams occur on fresh surfaces as brownish, irregular streaks but appear black on weathered surfaces, and are abundant in the lowermost outcrop layers of lagoonal facies of the lower outcrop layers of finely crystalline, microspar dolomite samples (Fig. 7 B). The seams are Fe oxidized stained but composed of dolomitic material, likely as a result of dolomite dissolution. Microstylolites that parallel laminae occur throughout sample A3 (Fig. 7 C). Stylolites are either dolomitic in composition or, when found along fractured bedding planes, are infilled with quartz, feldspars, and iron oxides.

4.2.3. Thrombolites

The thrombolites exhibit clotted, irregular microtextures (Fig. 7 A1 and A2). Rounded microcline and orthoclase, and sub-rounded quartz occur throughout the sample, with sparse amounts of peloids and ghost grains. SEM/EDS reveals minor mineral components of Fe-oxides and pyrite grains. The detected metal oxide morphologies range from euhedral to highly deformed in shape, and the pyrite has round to sub-round edges (Fig. S2 in supplementary material).

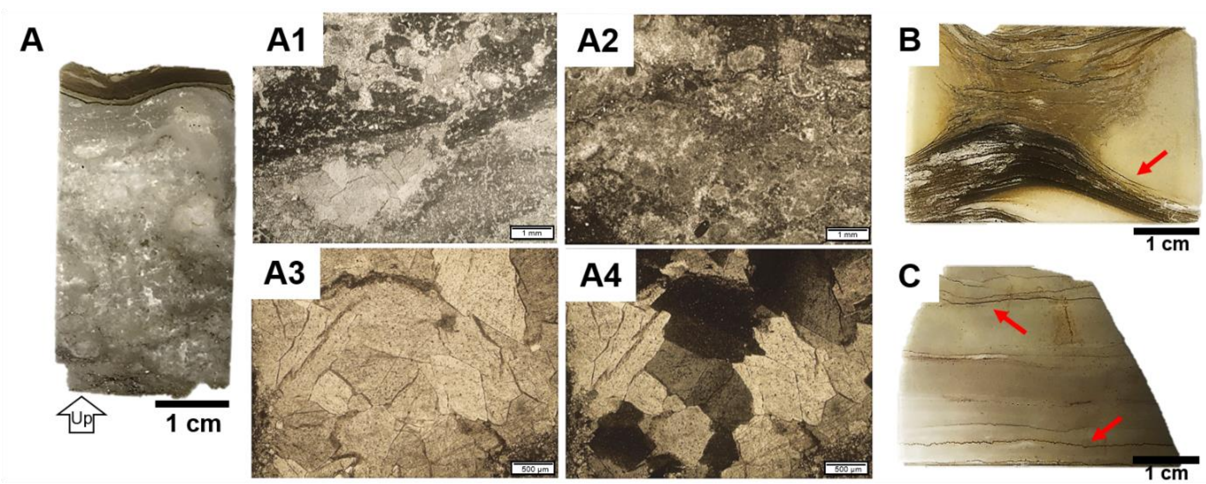

Fig. 7 Subtidal lagoonal facies microtextures**.** (A) Thin section of thrombolite sample. (A1) Plane polarized light (ppl) 2.5x magnification of clotted structure and large saddle dolomite-filled vug. (A2) Ppl 2.5x magnification of clotted thrombolite structure. (A3) Ppl 5x magnification of large saddle dolomite filled vug, indicative of burial dolomitization. (A4) Cross polarized light (xpl) of (A3) shows sweeping extinction characteristic of saddle dolomite. (B) Thin section of dolosiltite sample (A1) with wispy solution seams (red arrow). (C) Thin section of dolosiltite sample (A3) with microstylolites (red arrows).

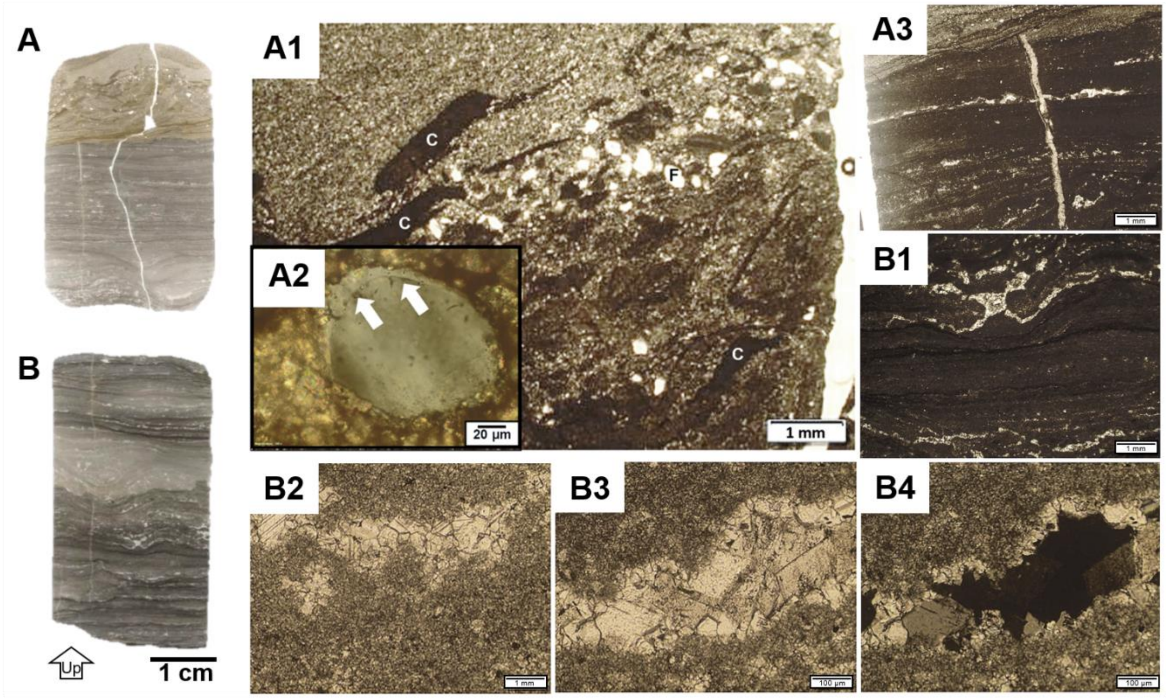

Fig. 8 Tidal flat stromatolitic facies microtextures. Thin sections of the top (A) and bottom (B) of a large domal stromatolite sample with corresponding photomicrographs: (A1) Plane polarized light (ppl) 2.5x magnification of rip-up clasts (marked C) and feldspars (marked F) within topmost portion of dome indicate a tidal channel deposit. (A2) Confocal Raman micrograph of an orthoclase overgrowth rim (white arrows) indicate thermal alteration. (A3) Ppl 2.5x magnification showing preservation of primary fenestral porosity that is crosscut by secondary microfracture porosity, evidence for early, near-surface dolomitization. (B1) Ppl 2.5x magnification showing very fine laminae of finely crystalline dolomite, common to tidal flat stromatolites. Fenestra (light colored areas in image) is filled with zoned and saddle dolomite. (B2) Ppl 2.5x magnification of microspar dolomite and coarser-grained zoned dolomite-filled fenestrae. (B3) Ppl 25x magnification of zoned and saddle dolomite-filled fenestrae surrounded by microspar. (B4) Cross polarized light (xpl) of (B3).

4.2.4. Ooids

The oolitic dolomite layers exhibit a dissolution-fill microstructural type of dolomite (Scholle and Ulmer-Scholle, 2003) with little or no original texture (radial, tangential, or otherwise) visible except for a dark-colored ooid outline and relics of concentric layers near the nucleus of the ooid (Fig. 9). Ooids vary in size from ~0.25 to 1 mm in diameter.

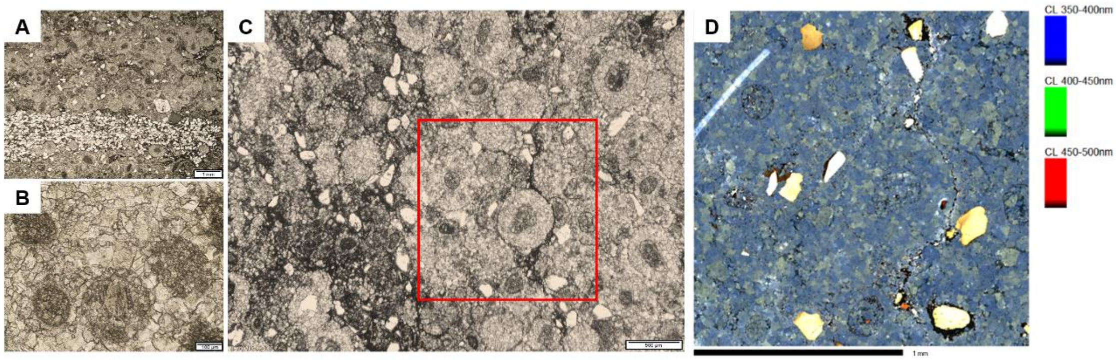

Fig. 9 Oolitic grainstone microtextures observed in thin sections. (A) Plane polarized light (ppl) photomicrograph 2.5x magnification of ooids (sample A10) with a finer-grained siliceous layer near the bottom of the image (white area). (B) Ppl photomicrograph 25x magnification of ooids from (A) showing dolomite replacement. (C) Ppl photomicrograph 5x magnification of CL mapped area (red box) in (D). (D) CL map showing characteristic violet luminescence. Bright white and yellow grains are feldspars.

4.2.5. Stromatolites

The microtexture of domal stromatolites is thinly layered convex-shaped layers of alternating dark (<1 mm thick) and light grey (≤1 cm thick) laminae (Fig. 8 A and B) and some very thin (<1 mm) layers appear black (Fig. 8 B). EDS showed no differences in composition between dark and light grey bands of laminae, however, the black laminae is enriched in felsic material. Primary fenestral porosity (≤1 mm thick) in the domal stromatolite is parallel to laminae and infilled with zoned and saddle dolomite. Very fine-grained, rounded intraclast rip-ups are situated on the topmost layer (Fig. 8 A1), which also contains large (<0.5 mm in diameter), rounded feldspars of microcline and orthoclase, and sub-rounded quartz grains. The orthoclase minerals exhibit overgrowth rims (Fig. 8 A2). The SEM/EDS reveals Ti-oxides, Fe-oxides, and apatite as minor mineral components (Fig. S2 in supplementary data).

4.3. Geochemistry

4.3.1. Bulk carbonate elemental analysis

Measurements by ICP-OES reveal that there is no major difference in bulk dolomite geochemistry across the samples among the Allentown layers except for the chert and feldspathic carbonate lithological outliers described in section 4.1 (A15 and A6). These layers exhibit relatively higher concentrations of Al, Cr, Fe, K, P, Ti, V, and Zn (Fig. 10 and Table S1 in supplementary material). ICP-OES reveals cherty layers contain 5x more titanium (Ti) than is detected in the other analyzed samples (Table S1 in supplementary material). Raman spectra show TiO_2 is predominantly anatase with minor amounts of rutile. Transition metals of Sr, Mo, Cu, Co, Ni, W, Cr, V are found in low concentrations (0.05 to 1.55 ppm) or are below detection limits (<DL). Na is detected in half of the samples (18.75 ppm average). The Mg/Ca stoichiometry values, average 0.53 ppm for all samples, excluding the values obtained from layers A15 and A6 (Fig. 4).

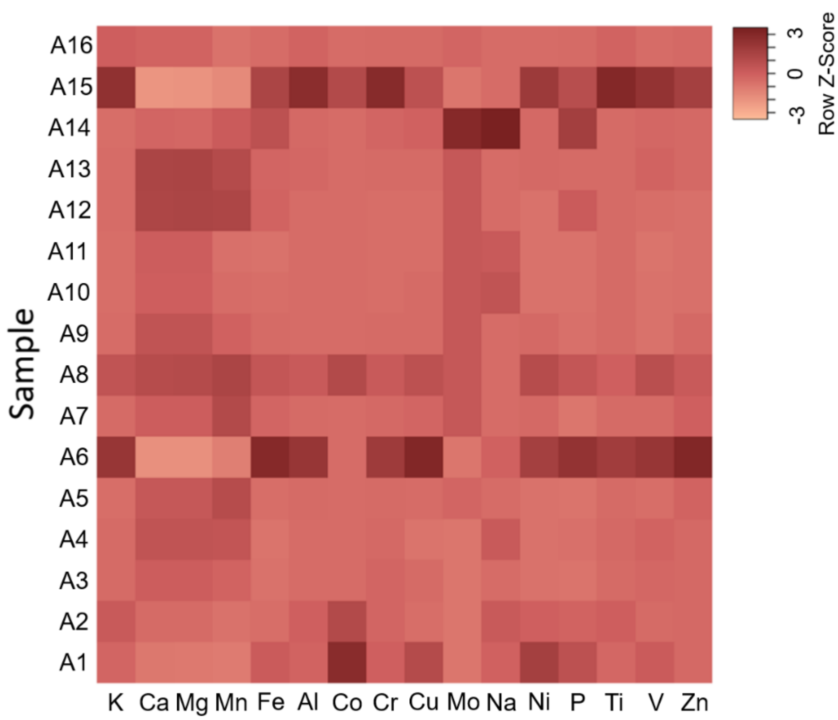

Fig. 10 ICP-OES bulk carbonate geochemical data. Composition heatmap of samples A1 to A16 (bottomost to topmost bedding). Row Z-score legend is the number of standard deviations from the mean (Z-score of 0 = the mean value). Cherty and feldspathic samples, A15 and A6, respectively, are enriched in various trace elements, as compared to dolomitic strata that does not differ much in bulk comparison.

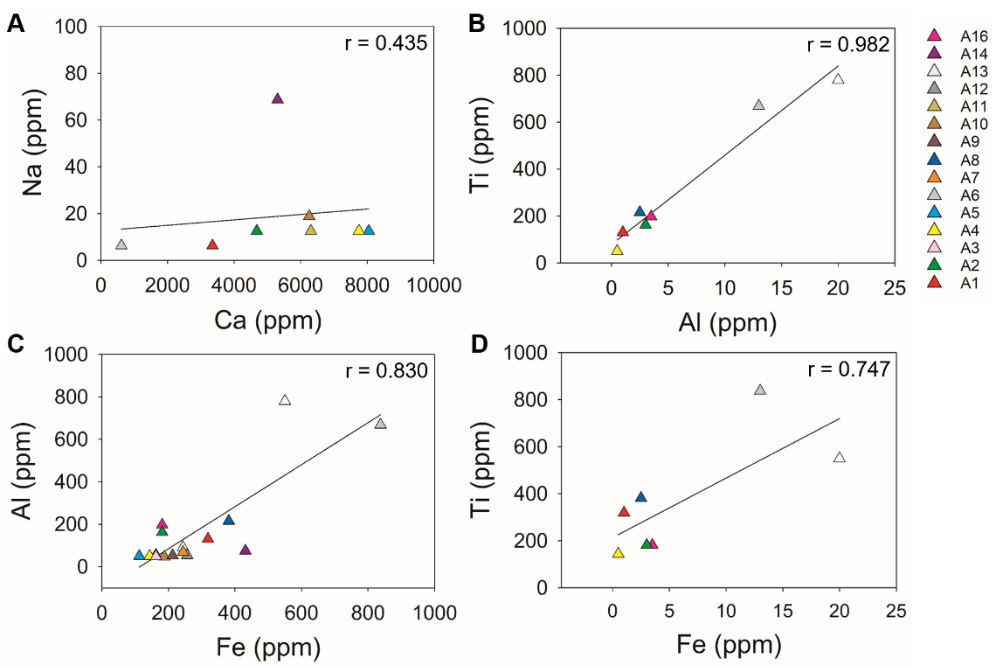

Fig. 11 ICP-OES results showing elemental relationships. (A) Weak correlation between Ca and Na. (B) Strong correlation between Al and Ti. (C) Strong correlation between Fe and Al. (D) Strong correlation between Fe and Ti. Bi-plots for (B) through (D) indicate that Al, Fe, and Ti are from the same lithogenous source(s).

4.3.2. Multi-generational dolomite high-resolution elemental analysis

Each generation of dolomite was targeted for microanalyses by electronprobe after identification with CL. All three generations of dolomite contain Zn and Mn, and the microspar and zoned dolomite generations have Si (Fig. 5 F). The zoned dolomite exhibits dark banding associated with Fe concentrations of 0.4 wt % or higher (Fig. 5 G). A compositional trend is observed in the microspar and zoned dolomite generations by a covarying increase in Si with a decrease in Ca and Mg. A decrease in Si abundance and an increase in Fe and Mn abundance is observed across each generation of dolomite. No Sr is detected in any generation. The cation ordering of Mg/Ca ratios averaged, 0.63 (n=116 spots analyzed), 0.63 (n=130), and 0.59 (n=131) wt % for microspar, zoned, and saddle dolomite generations, respectively (Table 1 and Table S2 in supplementary material).

4.3.3. Carbonate $\delta^{18}O$ and $\delta^{13}C$ composition

Isotope analysis reveals relatively low values of $\delta^{18}O_{dolo}$ (‰ VPDB) and $\delta^{13}C_{dolo}$ (‰ VPDB). Oxygen isotopes ($\delta^{18}O_{dolo}$) range from -18.23‰ to -6.05‰ referenced to VPDB with an average standard deviation of 0.39‰ (Fig. 12 and Table S3 in supplementary material). Inorganic carbon isotopes ($\delta^{13}C_{dolo}$) range from -6.54‰ to -0.84‰ referenced to VPDB with an average standard deviation of 0.33‰.

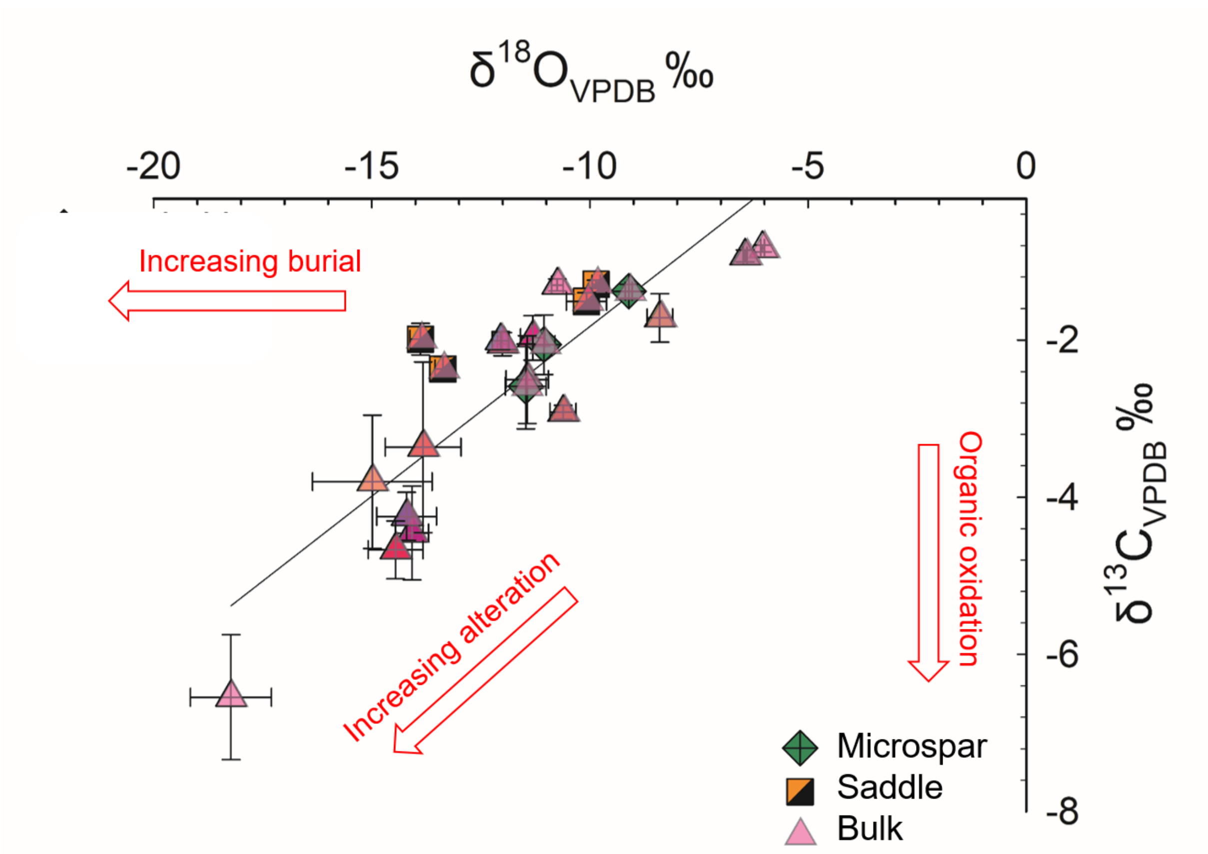

Fig. 12 The $\delta^{13}C_{dolo}$ and $\delta^{18}O_{dolo}$ compositions measured from bulk and micro-drilled microspar and saddle dolomite generations overlap. Alteration trends are marked by red arrows. Modified from Allan and Wiggins (1993). The positive covariance in isotopes (r=0.85) indicates alteration from mixed meteoric and marine fluids, and the low isotopic values trend is indicative of thermal alteration from burial dolomitization.

4.3.4. Total organic carbon and organic $\delta^{13}C$ composition

Elemental analysis shows that nitrogen abundance is below detection limits, and organic carbon abundance is 0.16 ± 0.45 weight percent with an average standard deviation of 0.002. Values of $\delta^{13}C_{org}$ for organic compounds range from -28.25‰ to -25.73‰ referenced to VPDB with an average standard deviation of 0.102 (Fig. 13 and Table S3 in supplementary material).

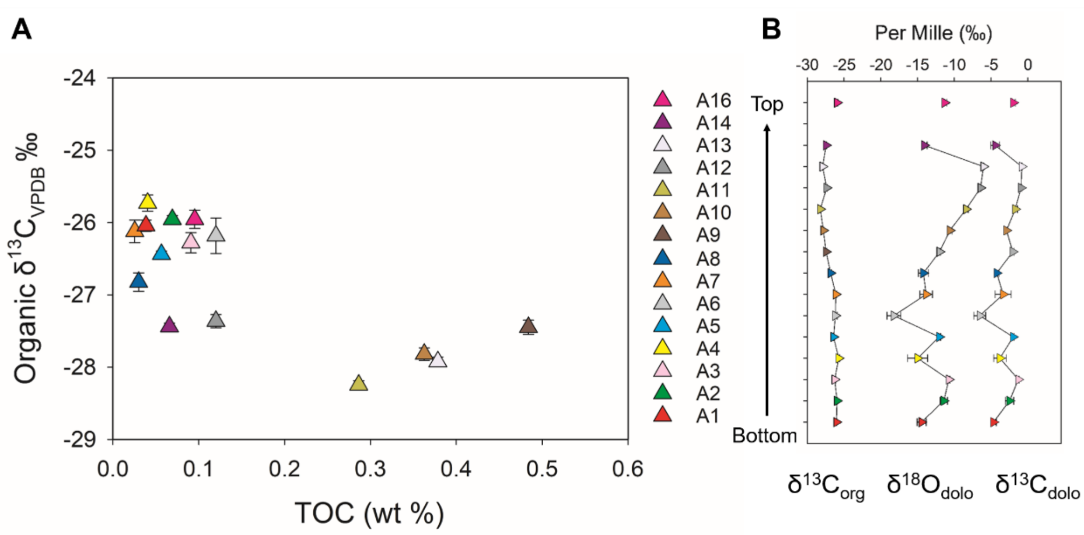

Fig. 13 Diagenetic alteration in isotopic trends and TOC**.** (A) Bi-plot of organic carbon abundances (weight percent) and organic carbon isotopic compositions indicating the effect of post-depositional alteration. (B) The $\delta^{13}C_{org}$, $\delta^{18}O_{dolo}$, and $\delta^{13}C_{dolo}$ isotopic trends across the outcrop reveal coupled $\delta^{18}O_{dolo}$ and $\delta^{13}C_{dolo}$ values, but $\delta^{18}O_{dolo}$ and $\delta^{13}C_{dolo}$ are decoupled with $\delta^{13}C_{org}$ isotopes, indicating post-depositional alteration of $\delta^{13}C_{dolo}$ values.

4.4. Confocal Raman microscopy and thermometry

Raman mapping of thin sections reveals that organic carbon, identified by D and G spectral bands, is exclusively associated with the microspar dolomite and commonly situated at or near grain boundaries. The D and G peaks show slight variations among peak intensity, peak area, and peak position (Fig. 14 and Tables S4a and S4b in supplementary material). D and G peak shifts within spectral maps are observed in samples A5 and A16, respectively (Fig. 15 B and Fig. S3 in supplementary material). *T*-test results reveal a statistical difference ($p<0.05$) in some D and G band positions and FWHM spectral values between stromatolite, thrombolite, and non-microbial macrostructure samples, as well as in the peak shifts observed in the stromatolite and thrombolite samples (Fig. S4 in supplementary material). Comparison of the cluster analysis and the Gaussian fitted data show that the results from the two methods are in good agreement with each other, but there is a broader range and relative standard deviation in data from the Gaussian fit method (Table 2). This variance in the Gaussian fitted spectra compared to the spectra from the cluster analysis may be due to more noise in the final spectrum of the background-subtracted Gaussian fitted peaks related to the difference in number of points selected by hand versus selected by computer in the cluster process. Cluster analysis shows D/G peak intensity ratios average 1.00 ± 0.05; D-FWHM averages 68 ± 34; and D-position averages 1334 ± 12. Gaussian fit analysis shows D/G peak intensity ratios average 1.02 ± 0.75; D-FWHM averages 47 ± 57; and D-position averages 1335 ± 26. All peak parameter results from the cluster and Gaussian fit methods are presented in supplementary material (Tables S4a and S4b), but the D-band parameters and their related thermometry will be the focus of this study's results and discussion.

Temperatures derived from Raman geothermometry averages 331°C ± 73 and D band variations show distinct grouping within samples in both peak position (rel cm^{-1}) and FWHM (Fig. 14). The sample grouping correlates to different temperature ranges: highest temperatures 368°C ± 11 in non-microbial samples; moderate temperatures 345°C ± 43 in stromatolite samples; low temperatures 305°C ± 12 in thrombolite samples (Fig. 14 B). Additionally, the thrombolite and stromatolite samples A5 and A16 exhibit peak shifts in D and G bands, respectively. These peak variations, spatially overlapping one another and occurring within the same mapped areas, suggest different degrees of crystallinity within the organic matter.

	I_D/I_G	G-FWHM	G position	D-FWHM	D position
Cluster					
Average	1.00	45.01	1600.54	68.42	1334.28
SD	0.01	3.48	5.29	13.91	4.11
Relative SD	1.40	7.74	0.33	20.33	0.31
Min	0.96	36.43	1594.66	49.06	1327.14
Max	1.02	50.33	1609.00	83.02	1339.00
Range	0.05	13.90	14.34	33.96	11.86
Gaussian fit					
	I_D/I_G	**G-FWHM**	**G position**	**D-FWHM**	**D position**
Average	1.02	44.21	1599.34	47.29	1335.40
SD	0.18	7.91	5.69	16.54	7.92
Relative SD	17.59	17.90	0.36	34.98	0.59
Min	0.70	25.17	1591.26	19.38	1321.59
Max	1.45	52.83	1608.52	75.88	1347.17
Range	0.75	27.66	17.26	56.50	25.58

Table 2. Average D and G band values obtained from the cluster and Gaussian fit methods showing comparable values among both peak processing methods used.

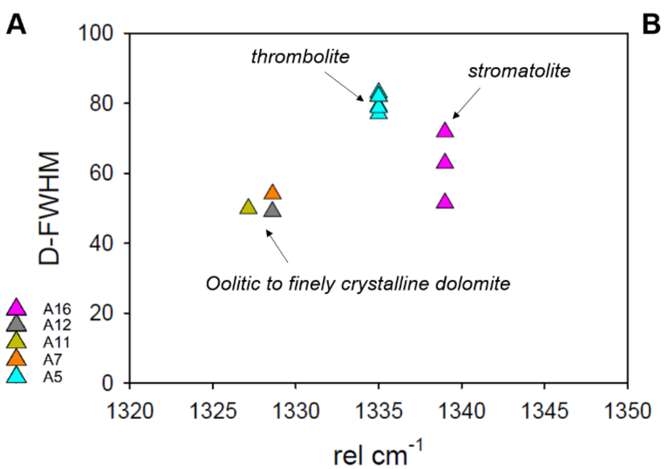

B

Sample ID	Sample Type	Temperature °C	T(°C) range
A16	Stromatolite	323.65 342.80 367.29	324°C - 367°C (345°C avg.)
A12	Oolitic Dolarenite	372.53	362°C - 373°C (368°C avg.)
A11	Dolarenite	370.71	
A7	Oolitic Dolosiltite	361.77	
A5	Thrombolite	312.43 307.91 308.67 299.52 301.76 301.73	300°C - 312°C (305°C avg.)

Fig. 14. Raman D band characteristics from cluster method. (A) Samples group together by general type. (B) Table of derived temperatures showing temperature variations based on grouping in (A).

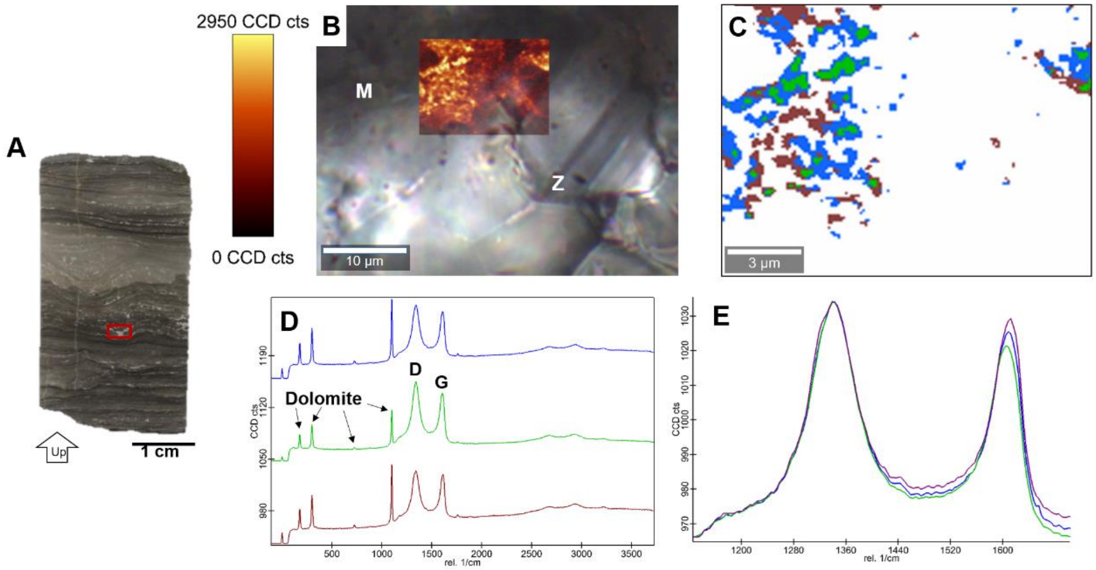

Fig. 15. Raman cluster method example. (A) Thin section of domal stromatolite (A16). Red box marks area mapped in (B). (B) Transmitted light micrograph of domal sample with overlay of Raman mapped D and G bands area. Bright yellow spots within the Raman map indicate spatial distribution of D and G bands before the cluster analysis. D and G bands are associated only with the microspar generation of dolomite (marked M) but not the zoned crystals (marked Z). (C) Raman map after cluster analyses showing differences in D and G bands averages and their spatial distribution. (D) corresponding spectra to cluster map (C) with dolomite and carbon peaks marked for reference. (E) overlay of D and G bands showing slight peak shift of G band which may indicate different levels of crystallinity.

5. DISCUSSION

The Allentown Formation consists entirely of dolomite, but the sedimentological evidence indicates a calcium carbonate precursor mineralogy in a shallowing upward peritidal sequence from a transitional marginal-marine setting (Wilson, 1975; Flügel, 2004). Characterization of the dolomitization setting, including fluid composition and temperature of formation, is fundamentally important when considering syngenicity of fossils within the host rock because the fossils should had experienced the same agents of alteration as the host rock. The following sections characterize the depositional environment and dolomitization based on outcrop observations, petrological, geochemical, and paleothermometry data, and in what measure the diagenetic history of the dolostone had affected the alteration of the organic carbon identified within the formation.

5.1. Sedimentary facies and paleoenvironment

Exposed stratigraphy displays a shallowing upward, or regressional, sequence where subtidal high energy ooid shoals transition to intertidal low energy lagoonal waters that progress to a supratidal mudcracked tidal flat (Fig. 1 C). The massive dolomitized oolitic grainstone beds are likely from ooid shoals that cut off marine waters and allowed for the development of lower energy lagoonal waters, which resulted in finer, silt-sized grained beds that overlay the grainstone. The lagoonal deposits are overlain by finely laminated domal stromatolites that co-occur with extensive near-shore, subaerial exposure evidence including mudcracks, collapse breccia, and tidal channel deposits. A near shore, shallow water setting is also indicated by high energy storm evidence throughout various beds recorded in edgewise conglomerate rip-up clasts, jumbled intraclasts, and torn laminae in small stromatolite domes (Fig. 2 E). Some layers of lagoonal dolosiltite contain sparse ooids, referred to as oolitic dolosiltite (Table 1), which are likely the result of wash-over deposition from ooid shoals during higher tides or storm events.

At the top of the outcrop, on the southwest side and adjacent to the large domal stromatolites, are extensive syneresis cracks (Fig. 2 N). Syneresis cracks form subaqueously (Plummer and Gostin, 1981), indicating that water levels may have been deeper on this side of the formation. Further lateral bedding changes are observed in microbial morphologies that are found towards the northeast side of the outcrop, but not visible from the southwest side of the outcrop. Vegetation cover limits correlations between lateral bedding differences, and therefore two stratigraphic columns were made, one for the southwest side of the outcrop (Fig. 3 column A) where bedding thickness is exactly measured, and one for the northeast side, where bedding thickness is approximated due to glacially polished surfaces (Fig. 3 column B). Column B depicts where the majority of the samples were collected and includes the various localities of microbial structures.

5.1.1. Microtexture and mineralogy

Petrographic microscopy of thin sections supports outcrop observational data. Microtextural tidal flat paleoenvironmental evidence is apparent in fine-grained dolomite crystals, finely layered stromatolitic laminae, and channel deposits with rip-up clasts and detrital feldspars and quartz (Scholle and Ulmer-Scholle, 2003). Similar light and dark grey layering in stromatolite structure have been reported as organic-poor to organic-rich layers (Grotzinger and Knoll, 1999; Bartley et al., 2000). Additionally, previous Allentown studies (Buie, 1932; Miller, 1941) have attributed the color alternation to differing amounts of organic matter and magnesium within the layers, stating that beds with high Mg weather to a lighter color while beds with lower Mg and more organic content undergo less change in color during weathering. These inferences cannot be confirmed here because EDS did not show a difference in Mg content within layers, and Raman mapping does not show a concentration of organic carbon content in the darker layers, instead data shows that these layers are rich in felsic material which is likely detrital residue of quartz and feldspars. The thin dark layers (<1 mm thick) of stromatolitic laminae may have formed during the periods of minor marine flooding when only the most minute particles were carried across the microbial mats (Wilson, 1975). Scattered siliceous fine grains are found along some stromatolitic laminae, and this feature is recorded in regression carbonate evaporitic cycles (Wilson, 1975). Although the lack of gypsum and anhydrite minerals in this outcrop does not support an evaporitic sabkha setting, the prolonged subaerial exposure may allow for freshwater flushing to removed evaporitic minerals and lower Sr and Na trace elements (Land, 1980). Freshwater evidence is supported by ooid microstructures, where coarse dolomite replaced the original calcium carbonate, which is consistent with freshwater dolomitization (Fig. 9).

5.1.2. Geochemical relationships with deposition and dolomitization

Geochemical evidence of freshwater input is revealed in bi-plots from ICP-OES data (Fig. 11). Calcium related to original limestone lithology shows a negative correlation with detrital mineral contributing elements of Fe, Al, Ti, and Na, related to feldspars, which indicate these are indeed terrigenous materials in the sampled dolostones (Ganai et al., 2018). The acid digestion, although targeted for carbonate minerals to determine ion substitution in the crystal lattice, may have partially dissolved oxide and silicate minerals (Voelz et al., 2019), or released fluvial derived cations that were adsorbed onto the carbonate mineral surface (Swart, 2015). Additionally, the ratios of Al/Ti (r=0.98 n=7), Fe/Al (r=0.83, n=16), and Fe/Ti (r=0.75, n=7) exhibit positive correlations indicating a single lithogenous source (Fig. 11 B through D), likely from the weathering products of inland rocks as previously interpreted (Witte and Monteverde, 2012; Dalton et al., 2014).

Additionally, petrological and SEM micrographs of rounded pyrite and feldspars support a detrital origin. These minerals make up minor constitutes in the whole rock and are most abundant in the chert and feldspathic carbonate layers. The pyrite is sub- to well-rounded, which is contrary to a previous study on a Pennsylvanian outcrop that reported cubic pyrite and interpreted this as an authigenic mineral (Miller, 1941). The distorted Fe- and Ti-oxides observed in this study (Fig. S2 in supplementary material) were likely altered before deposition and therefore are not indicative of strain or stress applied to the study area.

The relative abundance of major and trace elements in dolomite, including the Mg/Ca ratio, Fe, Mn, Zn, Sr, Na, and Si concentrations, can reveal the dolomitizing fluid’s origin and the formation setting (Morrow, 1982; Tucker and Wright, 1990; Gasparrini et al., 2006; Zhang et al., 2009; Guido et al., 2018). During carbonate diagenesis, concentrations of Sr and Na decrease and Fe, Mn increase (Wright and Tucker, 1990; Allan and Wiggins, 1993; Warren, 2000). The presence of Sr and Na is considered a signature of original seawater (Land, 1980; Allan and Wiggins, 1993) and dolomite formed in the presence of oxidizing surface waters, while Fe and Mn are signatures of reducing pore water in burial settings (Wright and Tucker, 1990). Traces of original precursory limestone from the Allentown formation have not been recorded (Dalton et al., 2014), but assuming the original limestone was deposited in Cambrian marine settings (Miller, 1941; Stead and Kodoma, 1984; Dalton et al., 2014), any detectable Sr and Na would indicate diagenetic alteration was relatively low and the dolomitization occurred in the presence of marine waters. No detectable Sr was found in any of the bulk carbonate samples or multi-generational dolomite spot analysis; therefore, any original seawater signature associated with Sr, if present, is below instrument detection limits. Although Na was detected in half (n=8) of the bulk carbonate samples analyzed from 68.75 ppm and 6.25 ppm, Na shows no correlation to Ca (Fig. 11 A) and is likely not related to the original seawater but could be from the alteration of Na bearing minerals, such as clays (Land, 1980; Kirmaci and Akdag, 2005; Li et al., 2015) that could have been adsorbed onto the carbonate mineral surface (Hu et al., 2005). The Allentown dolostone likely lost its Sr and Na trace element composition when it dolomitized in the presence of freshwater (Land, 1980; Allan and Wiggins, 1993). Trace element geochemistry is further discussed in sections 5.2.1.1. through 5.2.1.3.

5.2. Dolomitization

Based on its formation pathway, dolomite may be primary or secondary. Primary dolomite is known to be microbially mediated at low temperatures (Bontognali et al., 2010; Zhang et al., 2015), while secondary dolomite forms by the dolomitization process and is the diagenetic product of calcium carbonate minerals (Machel, 1978; Guido et al., 2018). Secondary dolomite starts by the formation of a metastable, non-stoichiometric magnesium calcium carbonate mineral phase from precursory calcite or aragonite minerals; this initial replacement starts with dissolution-re-precipitation and typically occurs in near-surface and shallow burial settings (Machel, 1978; Kupecz et al., 1993; Gregg et al., 2015). Over time, and often in deeper burial setting, recrystallization of the non-stoichiometric mineral phases will form stable, stoichiometric dolomite phases (Machel, 1978; Kupecz et al., 1993; Warren, 2000; Kaczmarek and Sibley, 2014; Gregg et al., 2015). Dolomite is considered stoichiometric and well-ordered when cations of magnesium and calcium reach a 1:1 ratio in alternating sheets within the carbonate crystal lattice (Machel, 1978). Therefore, secondary dolomite that is stoichiometric and has an ordered cation arrangement is considered to be diagenetically replaced, or, recrystallized. Although a recent study reported primary precipitation of stoichiometric and ordered dolomite from low temperature (27°C) using cultured anaerobic photosynthetic biofilm in conditions relevant to Archean seawater (Daye et al., 2019), stoichiometric and ordered dolomite has not yet been synthesized in the laboratory by abiotic, secondary dolomite precipitation at such low temperatures (Land, 1998; Gregg et al., 2015). Instead, the successful synthesis of secondary dolomite results from greater than 100°C (high) temperature experiments where the precursory calcium carbonate minerals undergo dissolution-re-precipitation to from disordered, high-magnesium calcitic phases before forming ordered dolomite (Kaczmarek and Sibley, 2014; Gregg et al., 2015). This ‘dolomite problem’ (Machel, 2004) leads to the hypothesis that massive beds of ordered, stoichiometric dolomite in the geologic record, are predominately the result of high temperature dolomitization of original calcitic carbonates. High temperatures dolomitization usually refers to greater than

100°C or 200°C (Kaczmarek and Sibley, 2014; Gregg, 2015), but temperatures as low as 50°C have been considered to be enough to alter original chemical signatures such as isotopic values and trace element concentrations (Gregg and Sibley, 1984; Warren, 2000). Even this type of low temperature dolomitization has been thought to alter original textural (Grotzinger and Knoll, 1999), and chemical signatures (Gregg and Sibley, 1984; Allan and Wiggins, 1993; Machel, 1997, Warren, 2000; Gregg et al., 2015; Kaczmarek and Sibley, 2014), and therefore may not be favorable for the preservation of original organic chemistry or body fossils (Schopf, 1999).

Experimental work has shown that stoichiometry increases with increasing Mg/Ca ratios in the fluid, and ordering increases over the reaction time; indicating that stoichiometry is associated with Mg concentration in the formation fluid and cation ordering is associated with the length of reaction time (Kaczmarek and Sibley, 2011). Accordingly, the level of diagenetic replacement within secondary dolomite can be inferred by both the dolomite's stoichiometry and degree of cation ordering. Stoichiometric dolomite has values of 2.89 Å d_{104}-spacing and 0.6 Mg/Ca ratios, and cation ordering of 0.40 or greater indicates relatively well-ordered dolomite. The average XRD d_{104}-spacing value for whole rock samples is 2.89 Å, which is indicative of stoichiometric dolomite (Table 1) (Goldsmith and Graf, 1958; Durocher and Al-Aasm, 1997). The average Mg/Ca ratio obtained for bulk carbonate is 0.53, and for each generation of dolomite 0.62. The degree of cation order in bulk rock samples ranges from 0.36 to 0.99, which indicates the samples are relatively well ordered and that the dolomitization was either a prolonged process (Kaczmarek and Sibley 2011) or involved a concentrated Mg ion solution (Sijing et al., 2014).

The Allentown dolomite does not retain evidence of the non-stoichiometric metastable magnesium carbonate minerals that are presumed to have formed during the initial dolomitization stages of the limestone replacement. The XRD d_{104}-spacing, Mg/Ca ratio, and cation ordering values (Table 1 and Fig. 4) are consistent and show that the Allentown dolomite from the analyzed outcrop is stoichiometric and ordered, and the original limestone formation has been entirely replaced by dolomite and fully recrystallized.

5.2.1. Multi-generational dolomite

Petrographic features, luminescence, and microprobe analyses suggest multistage dolomitization. Dolomite petrography shows three texturally different crystal types that are compositionally different, as revealed by CL and EPMA analyses. Determining the order of dolomite crystal formation is essential to reconstruct the paragenetic sequence and to reveal if chemical, thermal, or textural overprinting by later crystal generations exists. The following sections discuss the interpreted formation of each generation of dolomite.

5.2.1.1. Microspar dolomite

The first generation of dolomite is a finely crystalline replacive dolomite typified by microspar-sized crystals (Folk, 1959) with an average crystal size of 20 microns. This secondary dolomite replaced the precursory micritic limestone that formed by the lithification of calcium carbonate minerals from the original marginal marine depositional setting. Microcrystalline textures in dolomite (<10 microns) are thought to be from waters supersaturated in Mg (Sibley, 1991; Allan and Wiggins, 1993) and are common to early near surface dolomitization, and microbial-related primary dolomite precipitation (Moore, 1989; Sibley, 1991; Allan and Wiggins, 1993); The microspar dolomite reported here is larger in crystal size due to the coarsening of original microcrystalline calcium carbonate minerals during dolomitization (Folk, 1959). This generation of dolomite exhibits nonplanar, irregular intercrystalline grain boundaries, which is a common textural characteristic of growth at temperatures greater than 50°C (Gregg and Sibley, 1984; Sibley and Gregg, 1987; Warren, 2000), however, this texture has also been observed to form in low temperature, subaerial environments in the presence of concentrated Mg ion solution which enables rapid nucleation of crystals during dolomitization (Sijing et al., 2014). Based on all other evidence that is in agreement with near surface, low temperature formation, the microspar dolomite's texture likely resulted from rapid crystal growth in the presence of concentrated Mg ion fluids.

The CL spectral peaks at 389 nm and 650 nm are due to intrinsic lattice defects in the CO_3^{2-} structure and the substitution of Mg^{2+} with Mn^{2+} into the carbonate lattice, respectively (Machel et al., 1991; Habermann et al., 1997; Richter et al., 2003). A peak shift is present at 389 nm and may be due to different types of crystallographic lattice defects such as ion vacancies and other point defects. Variations in crystallographic defects may account for the variations in CL colors of increasing wavelength from blue, grey, to gold. Further, the three observed CL colors are found in the first two generations (microspar and zoned) of dolomite which are both interpreted to have formed in the early meteoric diagenetic realm, which may suggest that this luminescence pattern is related to the dolomite's formation path. Although rarely reported (Kusano et al. 2014), this violet-blue range of luminescence is known to occur in calcite and dolomite minerals that lack impurities (Machel et al., 1991), because the Allentown dolomite contains Si, Mn, Fe, and Zn impurities, the luminescence character is likely attributed to intrinsic crystallographic defects.

5.2.1.2. Zoned dolomite

Zoned dolomite occurs as small rhombohedral shaped crystals that infill pore space within the microspar dolomite (Fig. 6 A), and larger cavity lining crystals with cloudy rhombic cores (Fig. 6 B). Although the rhombohedral dolomite may have precipitated directly from fluids saturated in Mg ions while the outcrop was subaerially exposed (Sibley, 1978), the presence of cloudy cores suggests later recrystallization. Preserved zonation in crystals is recorded stages of primary crystal growth and relates to the fluctuating pore water chemistry during formation, a feature observed in dolomites formed during meteoric diagenesis (Allan and Wiggins, 1993). The zonation growth stages of primary precipitation alter between Ca:Mg zones that record mixed water influx likely from fresh and marine waters, to Fe:Mg zones that record reducing conditions from likely stagnant fluids (Katz, 1971). These growth stages may be related to the storm events recorded in bedding layers (see sections 2.2. and 5.1.) because only Fe^{2+} is incorporated into the carbonate lattice by replacing the Mg^{2+} in lattice sites (Katz, 1971; Allan and Wiggins, 1993); this oxidized state of Fe indicates that the dark bands of zonation formed during strong reducing conditions of stagnant fluids, and the light bands of zonation formed after storm events flushed the system and oxygenated the water leaving no soluble ferrous iron in solution, allowing the Ca:Mg zones to form (Katz, 1971).

The zoned dolomite exhibits the same CL characteristics as the microspar dolomite and may represent penecontemporaneous formation with the microspar dolomite, from the same type of meteoric fluids. Conversely, formational fluids may have interacted by causing minor dissolution of the microspar dolomite and released Mg and Si to be recycled into the zoned generation (Goodell and Garman, 1969; Land et al., 1975). Both scenarios could explain the Si present in the zoned dolomite, which is absent from the saddle dolomite.

5.2.1.3. Saddle dolomite

Saddle dolomite occurs as void-filling centers in primary fenestral pores and secondary microfractures and vugs. The dull luminescence, Fe-rich chemistry and saddle shape are all features of late stage, high temperature dolomite formation (Allan and Wiggins, 1993). This dolomite phase may be primary precipitated or replacive, but the lack of calcite relics indicates it is a primary cavity-fill phase (Mehmood et al., 2018). Observational crosscutting evidence at the outcrop is limited to one large saddle-filled vug that an overlying stylolite collapsed into and is surrounded by the infilling saddle dolomite (Fig. 2 Q). This suggests a penecontemporaneous formation of the two, and the saddle dolomite may have incorporated Mg from microspar dolomite after dissolution from stylolization during increasing overburden pressure that released Mg into the burial fluids (Goodell and Garman, 1969; Land et al., 1975). This Mg recycling could explain why stable oxygen isotope compositions overlap in all three generations of dolomite. The formational burial setting of saddle dolomite suggests it formed in a rock-buffered, isotopically closed system where pore fluids were, at least partially, composed of Mg provided from the penecontemporaneous dissolution of the host rock's microspar dolomite during localized stylolization (Gray et al., 1991; Oehlert and Swart, 2014) This final stage of dolomite formation thermally overprinted the entire formation as revealed from the light stable oxygen isotope composition (see 5.2.2.) and organic carbon Raman D and G bands (see 5.3.2.).

5.2.2. Carbonate $\delta^{18}O$ and $\delta^{13}C$ composition

The positive covariance (r=0.87 n=15 [bulk]; r=0.96 n=3 [microspar]) in $\delta^{18}O$ and $\delta^{13}C$ values suggests dolomite formation in a mixing zone of ^{18}O and ^{13}C-enriched and ^{18}O and ^{13}C-depleted water sources (Allan and Matthews, 1982; Allan and Wiggins, 1993; Oehlert and Swart, 2014). A comparison of results from the micro-drilled saddle and microspar samples shows that these values cannot be differentiated from bulk carbonate sample results as they fall within the range of error bars (Fig. 12). This may be due to the fact that the majority of the bulk sample is composed of microspar dolomite, and therefore the diagenetic trend of this dolomite phase dominates. The low $\delta^{18}O_{dolo}$ values (-18.23‰ to -6.05‰ VPDB) are likely from the late stage saddle dolomite which formed in deeper burial (Allan and Wiggins, 1993; Haas et al., 2017; Al-Aasm and Crowe, 2018) and at higher temperatures than the microspar and zoned dolomite.

The low values of $\delta^{13}C_{dolo}$ (Fig. 12) are from alteration during dolomitization and likely signifies the presence of organics in the system (Irwin et al., 1977; Schidlowski, 1988; Allan and Wiggins, 1993; Lamb et al., 2006). $\delta^{13}C_{dolo}$ values of -6‰ VPDB indicate thoroughly altered isotopic compositions from diagenesis in open systems with high water:rock ratios (Lohmann, 1988; Sharp, 2007).

Coupled $\delta^{18}O_{dolo}$ and $\delta^{13}C_{dolo}$ isotopes suggest that alteration for both the carbon and oxygen isotopes for all samples is contemporaneous and originates from the same source(s) (Fig. 13 B) (Des Marais et al., 1992; Jiang et al., 2012). The decoupled trends of $\delta^{13}C_{org}$ with $\delta^{18}O_{dolo}$ and $\delta^{13}C_{dolo}$ are likely related to diagenetic alteration and indicate the system was not rock buffered and does not retain the original $\delta^{13}C_{dolo}$ signature (Grotzinger et al., 2011; Jiang et al., 2012; Oehlert and Swart, 2014). Supporting this is the interpretation that the microspar and zoned dolomite formed in an early diagenetic setting of meteoric dolomitization, which is an isotopically open system (Gregory et al., 1989) where large amounts of fluids interacted with the rock and shifted $\delta^{13}C_{dolo}$ values to lighter values (Lohman, 1988; Sharp, 2007; Oehlert and Swart, 2014). Therefore, the decoupled $\delta^{13}C_{org}$ and $\delta^{13}C_{dolo}$ values indicate that diagenesis altered $\delta^{13}C_{dolo}$ values during exposure to freshwater, and this high fluid to rock ratio is responsible for the decoupled signature (Grotzinger et al., 2011; Jiang et al., 2012; Oehlert and Swart, 2014).

5.3. Characterization of organic carbon

Organic carbon is characterized here using TOC, $\delta^{13}C_{org}$, Raman mapping, and D and G peak analyses to determine alteration setting, spatial relationships between organic matter and minerals, and thermal maturity.

5.3.1. TOC and $\delta^{13}C_{org}$

The samples with higher TOC concentrations (0.484 to 0.286 wt %) have lighter $\delta^{13}C_{org}$ compositions, while samples with lower TOC (approximately 0.056 wt %) show heavier $\delta^{13}C_{org}$ compositions (Fig. 13 A). Such a decrease in TOC coupled with lighter $\delta^{13}C_{org}$ values is indicative of post-depositional thermal degradation (McKirdy and Powell, 1974; Strauss and Beukes, 1996; Eigenbrode and Freeman, 2006; Jiang et al., 2012). Oolitic dolosiltite sample A9 has the highest TOC at 0.48 wt %; this sample is dark grey microspar dolomite associated with rip-up clasts. Rip-up clasts appear periodically throughout the outcrop and are indicative of tidal channel deposits which may have deposited during storm events. The increase in TOC within samples A9, and oolitic dolarenite samples A10, A11, and oolitic dolosiltite sample A13, all of which include high energy, storm evidence of rip-up clasts and edge-wise conglomerates, suggests the possibility of terrestrial organic input that washed in during storms and was incorporated in the sediments and stromatolitic laminae during deposition.

The values of $\delta^{13}C_{org}$ range from -25.73 ‰ to -27.95 ‰ relative to VPDB (Fig. 13 B), which is consistent with organic input from decaying organic matter or microbial metabolism (Irwin et al., 1977; Schidlowski, 1988; Allan and Wiggins, 1993; Lamb et al., 2006)

5.3.2. Raman mapping and thermometry

The spatial relation of the organic carbon to multi-generational dolomite is significant for determining if the carbon was already in place before dolomitization, and therefore syngenetic with the Cambrian stromatolites. Confocal Raman microscopy reveals that D and G bands of organic carbon are only present in the first generation of dolomite and situated at or near grain boundaries.

The use of oxygen isotope ratios in carbonate minerals as a geothermometer (Friedman and O'Neil, 1977; Allan and Wiggins, 1993) is not justified here because measured oxygen isotopes values and geochemical data indicates that dolomitization did not take place in marine settings, but rather meteoric and burial settings which had reset the isotopic seawater values. Additionally, the late stage burial dolomitization thermally overprinted previous generations, obliterating the original dolomitization temperature (Land, 1980; Sharp, 2007) of the microspar dolomite. Therefore, calculated formation temperatures using a Cambrian marine baseline would be erroneous for this sample set and not indicative of the maximum burial temperature.

However, the color alteration index (CAI) of conodont fossils has shown to be a useful geothermometer to determine thermal maturity in sedimentary rock (Epstein et al., 1977; Marshall et al., 2001). Harris et al. (1995) report few conodont fossils (1-10 elements per kilogram of rock) were found in Warren and Sussex counties of New Jersey Allentown outcrops and those were poorly preserved texturally, deformed and fractured. The conodont fossils found have CAI (Epstein et al., 1977; Helsen et al., 1995) values of 5 that indicate that the Allentown dolomite reached temperatures of at least 300°C and burial depths of at least 10 km (Harris et al., 1995). Burial depths around 10 km would indicate burial pressure was at least 300 MPa (Tilley, 1924). Based on our outcrop observations and microtextural evidence, this outcrop had not been exposed to unidirectional stress that would align or elongate grains, but the pressure was likely lithostatic and uniform pressure derived from the burial process. However, the burial pressure had likely created the vertical microfractures observed in some layers (see 4.2.2.) Similarly, Stead and Kodama (1984), reported that Pennsylvanian Allentown outcrops likely reached minimum temperatures of 200-300°C because younger, Ordovician rocks that had not been as deeply buried as the Allentown contain conodont fossils with CAI values of 3.5-5. Although there may exist regional differences in tectonic settings that operated between Pennsylvania and New Jersey or different stratigraphic levels of the Allentown formation that were sampled in those studies compared to this study, the use of conodonts as a geothermometer for the dolomitization of the Allentown is useful and comparable to the Raman thermometry method used in this paper.

Organic carbon first-order bands of Raman spectra, (D and G bands at ~1350 and 1600 cm^{-1}, respectively) record the host rock's maximum temperature and can be used as an organic paleothermometer (Pasteris and Wopenka, 1991; Wopenka and Pasteris, 1993; Marshall et al., 2001; Marshall et al., 2012). The G band is the ordered, graphitic structure of carbon, and the D band is the disordered carbon structure. Variations in the bands, related to differing amounts of thermally induced rearrangement, can be used to determine structural order of the carbon and associated temperature setting required for such level of crystallinity (Pasteris and Wopeneka, 1991; Beyssac et al., 2002). Although there is currently no agreement on how to process peak data for thermometry studies, the geothermometer from Kouketsu et al. (2014) were used to compare results to the maximum alteration temperature inferred from previous conodont studies and determine if a similar thermal alteration between the host rock and organics exists.

Calculated temperatures yield a range of 300°C - 373°C (±30°C) which places the Allentown organic carbon within the medium-grade carbonaceous material temperature alteration zone of 280°C - 400°C. This medium-grade type of organic carbon alteration is also reflected in the overall D and G band spectral characteristics which exhibit D3 and D4 bands, and commonly have D and G bands that are equal in intensity (Table 2 and Tables 3a and 3b in supplementary material). These derived temperatures from collected Raman data corroborate the same temperature of thermal alteration as the dolomitization setting previously established using the conodont fossil CAI geothermometer.

5.3.3. Syngenicity and Indigeneity

Based on the spatial association with dolomite grains, and exclusive occurrence in the replacive microspar dolomite, the organic carbon was likely in place during dolomitization -previously trapped during the original limestone lithification (Fig. 15 B and Fig. S3 in supplementary material). This early dolomitization likely occurred penecontemporaneously with the lithification of limestone, from fluids supersaturated in Mg ions from seawater and freshwater mixing, that it rapidly produced stoichiometric dolomite, which as a thermodynamically stable phase, resisted further alteration and preserved the Cambrian organics by basically locking the first generation to prevent later fluid contaminations from entering. The placement of organic carbon suggests it is indigenous and syngenetic to the primary fabric of the host rock. The Raman cluster maps show the peak variations overlap spatially, suggesting all three varieties of organics were in place at the same time and the matching the alteration temperature with the host rock. All of these characteristics indicate that organic molecules are indigenous and syngenetic to the Cambrian dolomitic stromatolites.

5.3.4. Biogenicity

Claims of biogenicity of organic carbon unrelated to cellular morphological evidence should be approached with caution. The finding of organic carbon with an isotopic composition that may be indicative of microbial metabolism is not an explicit line of evidence for biogenicity (Braiser et al., 2003; De Gregorio and Sharp, 2006). Organic molecules can form from abiotic, autochthonous chemical reactions such as Fischer-Tropsch type processes in hydrothermal environments and decarbonation during metamorphism (McCollom and Seewald, 2006; Galvez et al., 2013; Bernard and Papineau, 2014). Although this null hypothesis cannot be fully rejected, there is no evidence of such hydrothermal processes in the outcopping area; and such a formational pathway was not likely present in this ancient coastal setting where it is interpreted that early dolomitization took place and preserved the organic carbon.

The evidence for Allentown organic carbon deriving from a biogenic origin are: 1) organic carbon is exclusive to the primary fabric (microspar dolomite) of the host rock which indicates a syngenetic origin, 2) the geological context is a marginal-marine setting with numerous microbial stromatolite macrostructures, 3) geochemical signals of $\delta^{13}C_{org}$ values are indicative of biology, and although the detection of disordered carbon by Raman spectroscopy is not alone indicative of biogenicity (Pasteris and Wopenka, 2003), the variations within D and G bands may be indicative of various alteration levels due to different types of starting material, of which one of more phases may be biological in origin.

The D and G peak differences may be due to different types of organic starting material that altered, or decomposed, differently despite undergoing the same alteration setting (Lamb et al., 2006). As an example, Lamb et al. (2006) reported organic matter in Holocene lagoonal and tidal flat sediments is mostly derived from suspended particulate organic matter such as plant detritus and phytoplankton from river and marine sources, respectively. Specifically, tidal flats are composed of a balanced mix between in situ organics and organics transported in by tides or rivers, both due to regular flushing or mixing of fresh and marine waters; lagoons are dominated by in situ organic sources due to isolation of waters (Lamb et al., 2006). This variation in tidal flat organics may potentially explain how three phases of organic carbon are found in the microbial samples (A16 and A5) and the lagoonal (A7) and ooid (A11 and A12) samples only have one carbon phase present (Fig. 14, Fig. 15, and Fig. S3 in supplementary material).

5.4. Paragenetic Sequence

5.4.1. Relative timing of dolomitization stages

Three stages of diagenesis have been outlined to explain the diagenetic phases observed in the Allentown Formation (Fig. 16). During stage 1, the Allentown Formation was deposited during the Late Cambrian in a transitional marginal marine setting. Facies produced in this peritidal environment rage from thinly-laminated stromatolitic, fine-grained lagoonal thrombolite, and massive oolitic grainstones. At the time of deposition, micritization of calcium carbonate grains during lithification of limestone occurred. The limestone dolomitized early in the marginal marine setting where freshwater mixed with marine water and produced microspar dolomite. Occurring contemporaneously, primary precipitation of dolomite rhombs that infill interparticle pores of microspar dolomite. During stage 2, increasing burial depth leads to microfracturing in selected layers of microspar dolomite, and recrystallization of some rhombic dolomite crystals. Mixed meteoric-marine fluids, alternating between oxidized and reduced conditions, produce zoned dolomite rims, while the original limestone is likely now completely dolomitized and stoichiometric. During stage 3, deeper burial produced late stage chemical compaction from overburden pressure resulting in stylolites, and localized dissolution seams that are concentrated in the lagoonal facies layers. A second stage of microfracturing occurs in select layers. Void filling dolomite precipitates in vugs, fractures, and fenestral pores by Fe- and Mn- rich, and likely reducing fluids.

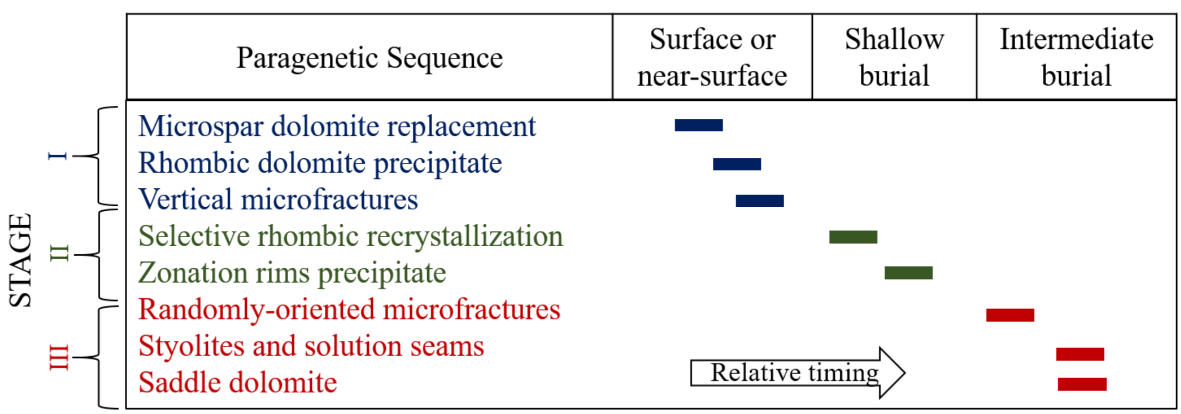

Fig. 16. Paragenetic sequence showing the formation of each dolomite generation with increasing burial depth. Modified from Hips et al. (2015).

5.4.2. Early dolomitization and preservation of organic carbon

Based on the mineral stoichiometry and cation ordering, the Allentown dolomite is completely recrystallized (Machel, 1978; Kupecz et al., 1993; Kaczmarek and Sibley, 2014; Gregg et al., 2015). The increase in Fe and Mn with each dolomite generation, undetectable Sr and Na concentrations, along with nonplanar crystal boundaries within microspar and saddle dolomite, zonation within the second generation, and saddle-shaped crystals within the third generation, all provide excellent evidence of the order and manner in which dolomitization process developed (Machel, 1978; Kupecz et al., 1993; Kaczmarek and Sibley, 2014; Gregg et al., 2015). The three generations of dolomite, although all subjected to the maximum burial temperature average of 331°C, preserved changes in the dolomitizing setting's fluid chemistry, which is apparent in CL color and EPMA spot analysis (see 5.2.1.).

A possible scenario for the Allentown's dolomitization and the relative timing of the development of each dolomite generation is presented here. Organic carbon is detected only within the first generation of microspar dolomite, at or near grain boundaries, and altered under similar burial and thermal conditions as the host rock. Organic material trapped in carbonate sediments during lithification will be displaced as the carbonate crystals grow larger and push organics between grain boundaries; thus, the organic carbon mapped was likely in place during the original lithification of limestone and before the microspar dolomite grains formed. The zoned dolomite precipitated directly from solution by infilling pore spaces within the microspar dolomite, and it exhibits the same luminescence of the microspar generation, suggesting this generation of dolomite may have precipitated penecontemporaneously with the microspar dolomite. As burial increased, temperature and pressure increased, and fluid chemistry changed to reflect Fe- and Mn-enrichment, recrystallizing the rhombohedral cores of the second dolomite generation before further precipitating outward in zonation rims of altering formation fluid, which remained preserved even during deeper burial and higher temperatures. The dull luminescence from the third generation of saddle dolomite differs from the first two dolomite generations and marks a different formational setting at a deeper burial, higher temperatures, and likely more reducing fluid signatures of elevated Fe- and Mn- trace elements in the dolomite lattice. The formation of the microspar and zoned dolomite led to decreased porosity of the host rock, which made the host rock impermeable to the later, deeper burial, and possibly hydrothermal in origin (Machel and Lonnee, 2002), saddle dolomite phase, and although thermally overprinted, did not chemically or structurally alter the microspar and zoned dolomite generations.

Stoichiometric dolomite is a thermodynamically stable phase of dolomite (Nordeng and Sibley, 1994) that is less susceptible to alteration by later diagenesis (Mueller et al., 2019). It is possible that the microspar and zoned dolomites were stoichiometric and thermodynamically stable before the formation of saddle dolomite and thus not susceptible to, further, deeper burial dolomitization. The sealing of the first microspar generation of dolomite by the second zoned generation of dolomite may be the reason why the organic carbon has remained preserved since the Cambrian.

6. CONCLUSIONS

Secondary, stoichiometric and ordered dolomite has been hypothesized to occur at either high temperatures or from multiple stages of recrystallization (Machel, 1978; Kupecz et al., 1993; Gregg et al., 2015) that would likely erase evidence of original texture, chemistry, and biology (Gregg and Sibley, 1984; Grotzinger and Knoll, 1999; Schopf, 1999; Warren, 2000). The results presented here indicate that stoichiometric and ordered dolomite can form within early dolomitization settings, undergo increasing temperature and burial diagenesis, and still retain syngenetic organic carbon. In summary:

- Outcrop observations (mudcracks, collapse breccia, rip-up clasts, edge-wise conglomerates) and petrological characteristics (finely-laminated stromatolites, fenestral porosity, rip-up clasts, finely crystalline microspar dolomite) reveal that the Allentown depositional setting was a tidal flat along the Cambrian coastline where original calcium carbonate mineral precursors dolomitized early in a marginal marine setting.
- The dolomite is ordered and all three generations of dolomite are stoichiometric and, therefore, fully recrystallized.
- Geochemical characteristics recorded by each generation of dolomite suggests two dolomitization processes dominated, mixing zone dolomitization in the meteoric diagenesis realm and burial dolomitization in the burial diagenesis realm.
- Microspar and zoned dolomite generations formed by dolomitization in a marine-meteoric mixing zone as revealed by the absence of evaporitic minerals and the presence of finely crystalline replacive dolomite crystals, as well as undetectable Sr and Na, and covariance in $\delta^{13}C_{dolo}$ and $\delta^{18}O_{dolo}$ values. Saddle dolomite formed by burial dolomitization as revealed by coarse void-filling crystals, dull luminescence, Fe and Mn enrichment, and low $\delta^{18}O_{dolo}$ values.
- The microspar and zoned dolomite were thermally overprinted by saddle dolomite during burial diagenesis. However, it did not overprint the formational chemistry of the previous two dolomite generations, suggesting that the burial was intermediate depth and temperatures and pressures were not high enough to obliterate previous generational dolomite that was likely stoichiometric and therefore thermodynamically stable, and not reactive to this final stage of diagenesis.

- Raman D and G bands indicate greenschist-like thermal maturity of organic carbon within the formation which is also suggested by conodont fossil CAI geothermometry from previous formational temperature studies of the Allentown dolostone.
- Organic carbon is found at or near grain boundaries, and only within the first generation of microspar dolomite. This suggests the organics were in place when the grains of dolomite formed, indicating a syngenetic origin of the organic carbon within the Cambrian stromatolites

Carbonate lithologies are diagenetically complex and their depositional and diagenetic setting will directly influence what biosignatures are preserved. This study reveals that dolomite that has undergone greenschist facies style thermal alteration can still retain original geochemical signatures necessary to reconstruct paragenesis, which along with outcrop observations, petrography, and Raman microscopy allows for the determination of biosignature syngenicity within ancient stromatolites that have been entirely diagenetically replaced by secondary dolomitization. The importance of this study is that preserved organic signatures, without cellular morphological support, can be used to determine syngeneity with host rock and open discussion for indigenous and biogenetic origins. This type of research is especially important when searching for life on other planets because microbial fossil preservation on Earth is rare, and different geologic environments and evolutionary histories on other planetary bodies will likely result in different types of life signatures recorded in the rocks. Terrestrial analogs such as this study will allow for better interpretations of potential biosignatures in Martian carbonates, which may have undergone varying levels of alteration. The Mars Perseverance Rover has the ability to target fine-grained carbonate rock, such as the microspar dolomite in this study, for Raman analysis, and if carbon is detected, these may serve as high potential biosignatures to be cached for future sample return mission(s).

7. ACKNOWLEDGMENTS

We are grateful to Alexander Gates and Michael Kalczynski for their assistance with field trip logistics and sample collection. This study was funded by NASA ASTEP (NNX14AT28G to M.G.) and NASA NAI ENIGMA – Rutgers University (80NSSC18M0093). The ICP-OES instrumentation used was purchased by NSF MI grant (EAR-1530582 to Ashaki Rouff). We thank Suah Yekeh for ICP-OES sample processing and data collection, supported by NSF REU (NSF-1459228 to Alexander Gates).

8. DATA AVAILABILITY

Supplementary data related to this article can be found at http://dx.doi.org/10.17632/k57gbw78d9.1, hosted at Mendeley Data (Murphy et al., subm).

9. REFERENCES

Al-Aasm, I. S., Crowe, R. 2018. Fluid compartmentalization and dolomitization in the Cambrian and Ordovician successions of the Huron Domain, Michigan Basin. Mar. Petrol. Geol. 92, 160-178.

Allan, J. R., Matthews, R. K. 1982. Isotope signatures associated with early meteoric diagenesis. Sedimentology 29, 797-817.

Allan, J. R., Wiggins, W. D. 1993. Dolomite reservoirs: geochemical techniques for evaluating origin and distribution, AAPG Continuing Education Course Notes No. 36.

Allwood, A. C., Walter, M. R., Kamber, B. S., Marshall, C. P., Burch, I. W. 2006. Stromatolite reef from the Early Archaean era of Australia. Nature 441, 714-718.

Ayllón-Quevedo, F., Souza-Egipsy, V., Sanz-Montero, M. E., Rodríquez-Aranda, J. P. 2007. Fluid inclusion analysis of twinned selenite gypsum beds from the Miocene of the Madrid basin (Spain). Implication on dolomite bioformation. Sed. Geol. 201, 212-230.

Barghoorn, E. S. Tyler, S. A. 1965. Microorganisms from the Gunflint Chert: These structurally preserved Precambrian fossils from Ontario are the most ancient organisms known. Science 147, 563-75.

Bartley, J. K., Knoll, A. H., Grotzinger, J. P., Sergeev, V. N. 2000. Lithification and fabric genesis in precipitated stromatolites and associated peritidal carbonates, Mesoproterozoic Billyakh Group, Siberia, in: Grotzinger, J. P., James, M. P. (Eds.), Carbonate Sedimentation and Diagenesis in the Evolving Precambrian World. SEPM Spec. Publ. 67, 59-73.

Bernard, S. Papineau, D. 2014. Graphitic Carbons and Biosignatures. Elements 10, 435-440.

Beyssac, O., Goffe, B., Chopin, C., Rouzaud, J. N. 2002. Raman spectra of carbonaceous material in metasediments: a new geothermometer. J. Metamorphic Geol. 20, 859-871.

Bontognali, T. R. R., Vasconcelos, C., Warthmann, R. J., Bernasconi, S. M., Dupraz, C., Strohmenger, C. J., McKenzie, J. A. 2010 Dolomite formation within microbial mats in the coastal sabkha of Abu Dhabi (United Arab Emirates). Sedimentology 57(3), 824-844.

Bragg, W. H. Bragg W. L. 1913. The Reflection of X-rays by Crystals. Proceedings of the Royal Society of London. Series A, Containing Papers of a Mathematical and Physical Character 88(605), 428-438.

Braiser, M., Green, O., Lindsay, J., Steele, A. 2003. Earth's oldest (~3.5 Ga) Fossils and the 'Early Eden Hypothesis': Questioning the Evidence. Origins Life Evol. Biosph. 34, 257-269.

Braiser, M. D., Antcliffe, J., Saunders, M., Wacey, D. 2015. Changing the picture of Earth's earliest fossils (3.5–1.9 Ga) with new approaches and new discoveries. PNAS 112, 4859.

Buick, R. 1990. Microfossil Recognition in Archean Rocks: An Appraisal of Spheroids and Filaments from a 3500 M.Y. Old Chert-Barite Unit at North Pole, Western Australia. Palaios 5(5), 441-459.

Buie, B. F. 1932. A Report of Investigations of the Allentown Limestone Formation. Thesis. LeHigh University, PA.

Calça, C. P., Fairchild, T. R., Cavalazzi, B., Hachiro, J., Petri, S., Huila, M. F. G., Toma, H.E., Araki, K. 2016. Dolomitized cells within chert of the Permian Assistência Formation, Paraná Basin, Brazil. Sed. Geol. 335, 120-135.

Dalton, R. F., Volkert, R. A., Monteverde, D. H., Herman, G. C., Canace, R. J. 2014. Bedrock Geologic Map of the Hamburg Quadrangle, Sussex County, New Jersey (1:24,000), New Jersey Geological and Water Survey, Trenton, NJ.

Daye, M., Higgins, J., Bosak, T. 2019. Formation of ordered dolomite in anaerobic photosynthetic biofilms. Geology 47(6), 509–512.

De Gregorio, B. T. Sharp, T. G. 2006. The structure and distribution of carbon in 3.5 Ga Apex chert: Implications for the biogenicity of Earth’s oldest putative microfossils. Amer. Miner. 91, 784-789.

Des Marais, D. J., Strauss, H., Summons, R. E., Hayes, J. M. 1992. Carbon isotope evidence for the stepwise oxidation of the Proterozoic environment. Nature 359, 605-609.

Drake Jr., A. A. 1965. Carbonate Rocks of Cambrian and Ordovician Age Northampton and Bucks Counties, Eastern Pennsylvania and Warren and Hunterdon Counties, Western New Jersey. Bull. US Geol. Surv. 1194-L.

Durocher, S. Al-Aasm, I. 1997. Dolomitization and Neomorphism of Mississippian (Visean) Upper Debolt Formation, Blueberry Field, Northeastern British Columbia: Geologic, Petrologic, and Chemical Evidence. AAPG Bull. 81(6), 954-977.

Ehlmann, B. L., Mustard, J. F., Murchie, S. L., Poulet, F., Bishop, J. L., Brown, A. J., Calvin, W. M., Clark, R. N., Des Marais, D. J., Milliken, R. E., Roach, L. H., Roush, T. L., Swayze, G.

A., Wray, J. J. 2008. Orbital Identification of Carbonate-Bearing Rocks on Mars. Science 322(5909), 1828-1832.

Eigenbrode, J. L. Freeman, K. H. 2006. Late Archean rise of aerobic microbial ecosystems. PNAS 103(43), 15759-15764.

Epstein, A. G., Epstein, J. B., Harris, L. D. 1977. Conodont Color Alteration – an Index to Organic Metamorphism. US Geol. Surv. Professional Paper 995.

Flügel, E. 2004. Carbonate Depositional Environments, in: Microfacies of Carbonate Rocks. Springer, Berlin, Heidelberg.

Folk, R. L. 1959. Practical petrographic classification of limestones. Bull. Amer. Assoc. Petrol. Geol. 43(1), 1-38.

Friedman, I. O'Neil, J. R. 1977. Compilation of stable isotope fractionation factors of geochemical interest. US Geol. Surv. Professional Paper 440-KK.

Galvez, M. E., Beyssac, O., Martinez, I., Benzerara, K., Chaduteau, C., Malvoisin, B., Malavieille, J. 2013. Graphite formation by carbonate reduction during subduction. Nature Geoscience 6, 473-477.

Ganai, J. A., Rashid, S. A., Romshoo, S. A. 2018. Evaluation of terrigenous input, diagenetic alteration, and depositional conditions of Lower Carboniferous carbonates of Tethys Himalaya, India. SESCI 3, 33-49.

Gasparrini, M., Bechstädt, T. Boni, M. 2006. Massive hydrothermal dolomites in the southwestern Cantabrian Zone (Spain) and their relation to the Late Variscan evolution. Mar. Petroleum Geol. 23, 543–568.

Goldsmith, J. R., Graf, D. L. 1958. Relation between lattice constants and composition of the Ca-Mg carbonate. Am. Mineral. 43, 84-101.

Goodell, H. G., Garman, R. K. 1969. Carbonate geochemistry of Superior deep test well, Andros Island, Bahamas. AAPG Bull. 53, 513-536.

Goudge, T. A., Mustard, J. F., Head, J. W., Fassett, C. I., Wiseman, S. M. 2015. Assessing the mineralogy of the watershed and fan deposits of the Jezero crater paleolake system, Mars. J. Geophys. Res. 120, 775-808.

Graf, D. L., Goldsmith, J. R. 1956. Some Hydrothermal Syntheses of Dolomite and Protodolomite. J. Geol. 64(2), 173-186.

Gray, D. R., Gregory, R. T., Durney, D. W. 1991. Buffered Fluid-Rock Interaction in Deformed Quartz-Rich Turbidite Sequences, Eastern Australia. J. Geophys. Res. 96(B12), 19,681-19,704.

Gregg, J. M., Sibley, D. F. 1984. Epigenetic dolomitization and the origin of xenotopic dolomite texture. J. Sediment. Petrol. 54, 908-931.

Gregg, J. M., Bish, D. L., Kaczmarek, S. E., Machel, H. G. 2015. Mineralogy, nucleation and growth of dolomite in the laboratory and sedimentary environment: A review. Sedimentology 62, 1749-1769.

Gregory, R. T., Criss, R. E., Taylor Jr., H. P. 1989. Oxygen isotope exchange kinetics of mineral pairs in closed and open systems: Applications to problems of hydrothermal alteration of igneous rocks and Precambrian iron formations. Chem. Geol. 75(1-2), 1-42.

Grotzinger, J. P., Rothman, D. H. 1996. An abiotic model for stromatolite morphogenesis. Nature 383, 423-425.

Grotzinger, J. P., Knoll, A. H. 1999. Stromatolites in Precambrian Carbonates: Evolutionary Mileposts or Environmental Dipsticks? Annu. Rev. Earth Planet. Sci. 27, 313-358.

Guido, A., Russo, F., Miriello, D., Mastandrea, A. 2018. Autochthonous Micrite to Aphanodolomite: The Microbialites in the Dolomitization Process, Geosciences 8, 451.

Haas, J., Hips, K., Bundai, T., Gyori, O., Lukoczki, G., Kele, S., Demeny, A., Poros, Z. 2017. Processes and controlling factors of polygenetic dolomite formation in the Transdanubian Range, Hungary: a synopsis. Int. J. Earth Sci. 106, 991-1021.

Habermann, D., Götze, J., Neuser, R., Richter, D.K. 1997. The phenomenon of intrinsic cathodoluminescence: Case studies of quartz, calcite and apatite. Zentralbl Geol Paläont Teil 1, Heft 10–12, 1275–1284.

Harris, A. G., Repetski, J. E., Stamm, N. R., Weary, D. J. 1995. Conodont Age and CAI Data for New Jersey. US Geol. Surv. Open-File Report 95-557.

Helsen, S., David, P., Fermont, W. J. J. 1995. Calibration of Conodont Color Alteration Using Color Image Analysis. J. Geol. 103, 257-267.

Hips, K., Haas, J., Poros, Z., Kele, S., Budai, T. 2015. Dolomitization of Triassic microbial mat deposits (Hungary): Origin of microcrystalline dolomite. Sed. Geol. 318(1), 113-129.

Horgan, B. H. N., Anderson, R. B., Dromart, G., Amador, E. S., Rice, M. S. 2020. The mineral diversity of Jezero crater: Evidence for possible lacustrine carbonates on Mars. Icarus 339.

Howell, B. F. 1945. Revision of Upper Cambrian faunas of New Jersey, Geological Society of America, Memoir 12.

Hu, C., Huang, J., Fang, N., Xie, S., Henderson, G. M., Cai, Y. 2005. Adsorbed silica in stalagmite carbonate and its relationship to past rainfall. Geochim. Cosmochim. Acta 69(9), 2285-2292.

Irwin, H., Curtis, C., Coleman, M. 1977. Isotopic evidence for source of diagenetic carbonates formed during burial of organic-rich sediments. Nature, 269.

Jiang, G., Wang, X., Shi, X., Xiao, S., Zhange, S., Dong, J. 2012. The origin of decoupled carbonate and organic carbon isotope signatures in the early Cambrian (ca. 542-520 Ma) Yangtze platform. Earth Planet Sci Lett. 317-318, 96-110.

Kaczmarek, S. E., Sibley, D. F. 2011. On the evolution of dolomite stoichiometry and cation order during high-temperature synthesis experiments: An alternative model for the geochemical evolution of natural dolomites. Sed. Geol. 240(1-2), 30-40.

Kaczmarek, S. E., Sibley, D. F. 2014. Direct physical evidence of dolomite recrystallization. Sedimentology 61, 1862-1882.

Katz, A. 1971. Zoned Dolomite Crystals. J. Geol. 79(1), 38-51.

Kirmaci, M. Z., Akdağ, K. 2005. Origin of dolomite in the Late Cretaceous-Paleocene limestone turbidites, eastern Pontides, Turkey. Sed. Geol. 181(1-2), 39-57.

Knoll, A. H. Strother, P. K., Rossi, S. 1988. Distribution and Diagenesis of Microfossils from the Lower Proterozoic Duck Creek Dolomite, Western Australia. Precambr. Res. 38, 257-279.

Kouketsu, Y., Mizukami, T., Mori, H., Endo, S., Aoya, M., Hara, H., Nakamura, D., Wallis, S. 2014. A new approach to develop the Raman carbonaceous material geothermometer for low-grade metamorphism using peak width. Island Arc 23, 33-50.

Kupecz J. A., Montanez I. P., G., Gao 1993. Recrystallization of Dolomite with Time, in: Rezak, R., Lavoie, D. L. (Eds.), Carbonate Microfabrics. Frontiers in Sedimentary Geology. Springer, New York, NY.

Kusano, N., Nishido, H., Inoue, K. 2014. Cathodoluminescence of calcite decomposed from dolomite in high-temperature skarn. J. Miner. Petrol. Sci. 109(6), 286-290.

Lamb, A. L., Wilson, G. P., Leng, M. J. 2006. A review of coastal palaeoclimate and relative sea-level reconstructions using $\delta^{13}C$ and C/N ratios in organic material. Earth Sci. Rev. 75, 29-57.

Land, L. S., Salem, M. R. I., Morrow, D. W. 1975. Paleohydrology of Ancient Dolomites: Geochemical Evidence. AAPG Bull. 59(9), 1602-1625.

Land, L. S. 1980. The isotopic and trace element geochemistry of dolomite: The state of the art, in: Zenger, D. H., Dunham, J. B., Ethington, R. L. (Eds.), Concepts and Models of Dolomitization. SEPM Spec. Publ. 28, 87-110.

Land, L.S. 1998. Failure to precipitate dolomite at 25°C from dilute solution despite 1000-fold oversaturation after 32 years. Aquat. Geochem. 4(3- 4), 361–368.

Li, Q., Jiang, Z., Hu, W., You, X. 2015. Origin of Dolomite in the Middle Triassic Zhouchongcun Formation, Central Lower Yangtze Region, Southeast China. Carpath. J. Earth Env. 10(1), 89-100.

Lindtke, J., Ziegenbalg, S. B., Brunner, B., Rouchy, J. M., Pierre, C., Peckmann, J. 2011. Authigenesis of native sulphur and dolomite in a lacustrine evaporitic setting (Hellín basin, Late Miocene, SE Spain). Geol. Mag. 148(4), 655-669.

Lohmann, K. C. 1988. Geochemical patterns of meteoric diagenetic systems and their application to studies of paleokarst, in: James, N. P., Choquette, P. W. (Eds.), Paleokarst. Springer-Verlag, New York, 58–80.

Machel, H. G. 1978. Dolomites and dolomitization, in: Sedimentology. Encyclopedia of Earth Science. Springer, Berlin, Heidelberg.

Machel, H. G., Mason, R. A., Mariano, A. N., and Mucci, A. 1991. CAUSES AND EMISSION OF LUMINESCENCE IN CALCITE AND DOLOMITE, in: Barker, C. E., Kopp, O. C. (Eds.), Luminescence Microscopy and Spectroscopy: Qualitative and Quantitative Applications. SEPM Short Course Notes, 25.

Machel, H. G. 1997. Recrystallization versus neomorphism, and the concept of 'significant recrystallization' in dolomite research. Sed. Geol. 113, 161-168.

Machel, H. G., Lonnee, J. 2002. Hydrothermal dolomite – a product of poor definition and imagination. Sed. Geol. 152(3-4), 163-171.

Machel, H. G. 2004. Concepts and models of dolomitization – a critical reappraisal, in: Braithwaite, C. J. R., Rizzi, G., Darke, G. (Eds.), The Geometry and Petrogenesis of Dolomite Hydrocarbon Reservoirs. Geol. Soc. London, Spec. Publ. 235, 7-63.

Marshall, A. O., Emry, J. R., Marshall, C. P. 2012. Multiple Generations of Carbon in the Apex Chert and Implications for Preservation of Microfossils. Astrobiology 12(2).

Marshall, C. P., Mar, G. L., Nicoll, R. S., Wilson, M. A. 2001. Organic geochemistry of artificially matured conodonts. Org. Geochem. 32, 1055-1071.

McCollom, T. M., Seewald, J. S. 2006. Carbon isotope composition of organic compounds produced by abiotic synthesis under hydrothermal conditions. Earth Planet Sci Lett. 243, 74-84.

McKirdy, D. M., Powell, T. G. 1974. Metamorphic Alteration of Carbon Isotopic Composition in Ancient Sedimentary Organic Matter: New Evidence from Australia and South Africa. Geology 2, 591-595.

Mehmood, M., Yaseen, M., Khan, E. U., Khan, M. J. 2018. Dolomite and Dolomitization Model – A Short Review. Int J Hydro. 2(5), 549-553.

Miller, B. L. 1941. LeHigh County Pennsylvania: Geology and Geography, Pennsylvania Geological Survey Bulletin, 4th Series C 39. Harrisburg, PA.

Monteverde, D.H. 1992. Bedrock geologic map of Sussex County, New Jersey, portions of the Culvers Gap and Lake Maskenozha quadrangles, New Jersey Geological Survey Geologic Map, 92-1.

Moore, C. H. 1989. Carbonate Diagenesis and Porosity, in Developments in Sedimentology, 46, Amsterdam, Elsevier, 46-338.

Morrow, D.W. 1982. Diagenesis II. Dolomite—Part II: Dolomitization Models and Ancient Dolostones. Geoscience Canada 9, 95-107.

Mueller, M., Igbokwe, O. A., Walter, B., Pederson, C. L., Riechelmann, S., Richter, D. K., Albert, R., Gerdes, A., Buhl, D., Neuser, R. D., Bertotti, G., Immenhauser, A. 2019. Testing the preservation potential of early diagenetic dolomites as geochemical archives. Sedimentology, 67(2), 849-881.

Mustard, J. F., Adler, M., Allwood, A., Bass, D. S., Beaty, D. W., Bell III, J. F., Brinckerhoff, W. B., Carr, M., Des Marais, D. J., Drake, B., Edgett, K. S., Eigenbrode, J., Elkins-Tanton, L. T., Grant, J. A., Milkovich, S. M., Ming, D., Moore, C., Murchie, S., Onstott, T. C., Ruff, S. W., Sephton, M. A., Steele, A., Treiman, A. 2013. Report of the Mars 2020 Science Definition Team, 154 pp., posted July 2013, by the Mars Exploration Program Analysis Group (MEPAG) at http://mepag.jpl.nasa.gov/reports/MEP/Mars_2020_SDT_Report_Final.pdf.

Nordeng, S. H., Sibley, D. F. 1994. Dolomite stoichiometry and Ostwald's Step Rule. Geochim. Cosmochim. Acta 58, 191-196.

Oehlert, A. M., Swart, P. K. 2014. Interpreting carbonate and organic carbon isotope covariance in the sedimentary record. Nat. Commun. 5, 1–7.

Pasteris, J. D., Wopenka, B. 1991. Raman spectra of graphite as indicators of degree of metamorphism. Can. Mineral. 20, 1-9.

Pasteris, J. D., Wopenka, B. 2003. Necessary, but not sufficient: Raman identification of disordered carbon as a signature of ancient life. Astrobiology 3(4), 727-38.

Plummer, P. S., Gostin, V. A. 1981. Shrinkage cracks: desiccation or synaeresis. J. Sediment. Petrol. 51, 147-1156.

Pratt, B. R., James, N. P., Cowan, C. A. 1992. Peritidal carbonates, in: Walker, R. G., James, N. P. (Eds.), Facies Models – Response to Sea Level Change. Geological Association of Canada, 303-322.

Rao, V. P., Kessarkar, P. M., Krumbein, W. E., Krajewski, K. P., Schneider, R. J. 2003. Microbial dolomite crusts from the carbonate platform off western India. Sedimentology 50, 819-830.

Richter, D. K., Götte, T., Götze, J., Neuser, R. D. 2003. Progress in application of cathodoluminescence (CL) in sedimentary petrology. Mineral. Petrol. 79(3-4), 127-166.

Sanz-Montero, M. E., Rodríquez-Aranda, J. P., García del Cura, M. A. 2008. Dolomite-silica stromatolites in Miocene lacustrine deposits from the Duero Basin, Spain: the role of organotemplates in the precipitation of dolomite. Sedimentology 55, 729-750.

Schidlowski, M. 1988. A 3,800-million-year isotopic record of life from carbon in sedimentary rocks. Nature 333, 313-318.

Scholle, P. A., Ulmer-Scholle, D. S. 2003. A Color Guide to the Petrography of Carbonate Rocks: Grains, Textures, Porosity, Diagenesis. AAPG Memoir 77.

Schopf, J. W. 1999. Cradle of Life: The Discovery of Earth's Earliest Fossils. Princeton University Press, Princeton, NJ.

Schopf, J. W., Kudryavtsev, A. B. 2012. Biogenicity of Earth's earliest fossils: A resolution of the controversy. Godwana Research 22(3-4), 761-771.

Sharp, Z. 2007. Principles of Stable Isotope Geochemistry. Pearson Prentice Hall.

Sibley D. 1978. Dolomite textures, in: Middleton, G. V., Church, M. J., Coniglio, M., Hardie, L. A., Longstaffe, F. J. (Eds.), Encyclopedia of Sediments and Sedimentary Rocks. Encyclopedia of Earth Sciences Series. Springer, Dordrecht.

Sibley, D. F., Gregg, J. M. 1987. Classification of Dolomite Rock Textures. J. Sed. Petrol. 57(6), 967-975.

Sibley D. F. 1991. Secular changes in the amount and texture of dolomite. Geology 19(2), 151-154.

Sijing, H., Keke, H., Jie, Lu, Yefang, L. 2014. The relationship between dolomite textures and their formation temperature: a case study from the Permian-Triassic of the Sichuan Basin and the Lower Paleozoic of the Tarim Basin. Pet. Sci. 11, 39-51.

Stead, R. J., Kodama, K. P. 1984. Paleomagnetism of the Cambrian Rocks of the Great Valley if East Central Pennsylvania: Fold Test Constraints on the Age of Magnetization, Plate reconstruction, in: Paleozoic paleomagnetism: Interim report of the Working Group 2 on Phanerozoic Plate Motions and Orogenesis. Washington, D. C.: American Geophysical Union.

Strauss, H., Beukes, N. J. 1996. Carbon and sulfur isotopic compositions of organic carbon and pyrite sediments from the Transvaal Supergroup, South Africa. Precambr. Res. 79, 57-71.

Sugitani, K., Grey, K., Allwood, A., Nagaoka, T., Mimura, K., Minami, M., Marshall, C. P., Van Kranendonk, M. J., Walter, M. R. 2007. Diverse microstructures from Archaean chert from the Mount Goldsworthy–Mount Grant area, Pilbara Craton, Western Australia: Microfossils, dubiofossils, or pseudofossils? Precambr. Res. 158(3-4), 228-262.

Swart, P. K. 2015. The geochemistry of carbonate diagenesis: The past, present and future. Sedimentology 62, 1233-1304.

Tilley, C. 1924. The Facies Classification of Metamorphic Rocks. Geological Magazine 61(4), 167-170.

Tucker, M., Wright, V. P. 1990. Carbonate Sedimentology. Black-Well Scientific Publications, Oxford.

Van Kranendonk, M. J., Webb, G. E., Kamber, B. S. 2003. Geological and trace element evidence for a marine sedimentary environment of deposition and biogenicity of 3.45 Ga stromatolitic carbonates in the Pilbara Craton, and support for a reducing Archaean ocean. Geobiology 1(2), 91-108.

Voelz, J. L., Johnson, N. W., Chun, C. L., Arnold, W. A., Penn, R. L. 2019. Quantitative Dissolution of Environmentally Accessible Iron Residing in Iron-Rich Minerals: A Review. ACS Earth Space Chem. 3, 1371-1392.

Warren, J. 2000. Dolomite: occurrence, evolution, and economically important associations. Earth-Sci. Rev. 52(1-3), 1-81.

Weller, S. 1903. The Paleozoic faunas: New Jersey Geological Survey Report on Paleontology, 3.

Wilson J. L. 1975. Carbonate Facies in Geologic History, Springer-Verlag, New York.

Witte, R. W., Monteverde, D. H. (2012) Geologic History of New Jersey's Valley and Ridge Physiographic Province, New Jersey Geological and Water Survey Information Circular, Trenton, NJ.

Wopenka, B., Pasteris, J. D. 1993. Structural characterization of kerogens to granulite-facies graphite: Applicability of Raman microprobe spectroscopy. Amer. Miner. 78, 533-557.

Zhang, F., Xu, H., Shelobolina, E. S., Konishi, H., Converse, B., Shen, Z., Roden, E. E. 2015. The catalytic effect of bound extracellular polymeric substances excreted by anaerobic microorganisms on Ca-Mg carbonate precipitation: Implications for the “dolomite problem”. Amer. Miner. 100(2-3), 483–494.

Zhang, J., Hu, W., Qian, Y., Wang, X., Cao, J., Zhu, J., Li, Q., Xie, X. 2009. Formation of saddle dolomites in Upper Cambrian carbonates, western Tarim Basin (northwest China): Implications for fault-related fluid flow. Mar. Petrol. Geol. 26, 1428-1440.